

1 **Assessing the rate of crustal extension by 2D sequential restoration analysis: a** 2 **case study from the active portion of the Malta Escarpment.**

3 Salvatore Gambino^{1*}, Giovanni Barreca^{1,2}, Felix Gross^{3,4}, Carmelo Monaco^{1,2,5} Marc-André Gutscher⁶,
4 G. Ian Alsop⁷

- 5 1) Department of Biological, Geological and Environment Sciences, University of Catania, Catania, Italy,
6 2) CRUST—Interuniversity Center for 3D Seismotectonics with Territorial Applications, Chieti, Italy,
7 3) Institute of Geosciences, Kiel University, Kiel, Germany,
8 4) Center for Ocean and Society, Kiel University, Germany, Kiel,
9 5) Istituto Nazionale di Geofisica e Vulcanologia, Osservatorio Etneo, Catania, Italy,
10 6) Laboratoire Géosciences Ocean, UMR6538 CNRS/University of Brest, Plouzané, France
11 7) Department of Geology & Geophysics, University of Aberdeen, Scotland, UK
12
13
14

15 **Corresponding Author (*)**

16 Salvatore Gambino
17 (salvatore.gambino@unict.it)

18

19 **Acknowledgments**

20 The bathymetric data were extracted from Gutscher et al., (2017) and from EMODnet open dataset
21 (<http://www.emodnet-bathymetry.eu/>). Digital topographic data are from the Japan Aerospace Exploration
22 Agency (<https://www.eorc.jaxa.jp>). The authors also acknowledge the use of MOVE Software Suite granted
23 by Petroleum Experts Limited (www.petex.com). This work is part of the S. Gambino's Ph.D. research project
24 at the University of Catania. Bernard Mercier de Lepinay (GeoAzur, Université de Nice/CNRS), is also
25 acknowledged for the CIRCEE-HR seismic data processing.

26 **Conflict of Interest**

27 The authors declare that the research was conducted in the absence of any commercial or financial relationships
28 that could be construed as a potential conflict of interest.

29 **Funding**

30 This work benefits from founding from the University of Catania in the framework of the project
31 "Multidisciplinary analysis of the deformation around active tectonic structures" (responsible G. Barreca) and
32 partly from the MUSE 4D project - Overtime tectonic, dynamic and rheologic control on destructive multiple
33 seismic events -Special Italian Faults & Earthquakes: from real 4D cases to models in the frame of PRIN 2017.

34 **Authors' contribution**

35 SG: work planning, conceptualization, seismic data interpretation, data analysis and interpretation of results,
36 review of literature, figures preparation, writing the initial draft and final version of the manuscript. GB:
37 seismic data interpretation, data analysis and interpretation of results, review of literature, writing the initial

38 draft and final version of the manuscript, critical reading of the manuscript, funding acquisition. FG: POS496
39 seismic data acquisition and processing, critical reading of the manuscript. CM: review of the literature data,
40 critical reading of the manuscript, funding acquisition, supervision, final approval of the manuscript. M-AG:
41 planned the CIRCEE marine geophysical survey, seismic data acquisition, critical reading of the manuscript.
42 GIA: critical reading of the manuscript, writing the final version of the manuscript, supervision, final approval
43 of the manuscript.

44

45

Abstract

46 Tectono-stratigraphic interpretation and sequential restoration modelling was performed over two
47 high-resolution seismic profiles crossing the Western Ionian Basin of southern Italy. This analysis
48 was undertaken in order to provide greater insights and a more reliable assessment of the deformation
49 rate affecting the area. Offshore seismic profiling illuminates the sub-seafloor setting where a belt of
50 active normal faults slice across the foot of the Malta Escarpment, a regional-scale structural
51 boundary inherited from the Permo-Triassic palaeotectonic setting. A sequential restoration workflow
52 was established to back-deform the entire investigated sector with the primary aim of analysing the
53 deformation history of the three major normal faults affecting the area. Restoration of the tectono-
54 stratigraphic model reveals how deformation rates evolved through time. In the early stage, the
55 studied area experienced a significant deformation with the horizontal component prevailing over the
56 vertical element. In this context, the three major faults contribute to only one third of the total
57 deformation. The overall throw and extension then notably reduced through time toward the present
58 day and, since the middle Pliocene, ongoing crustal deformation is accommodated almost entirely by
59 the three major normal faults. Unloading and decompaction indicate that when compared to the
60 unrestored seismic sections, a revision and a reduction of roughly one third of the vertical
61 displacement of the faults offset is required. This analysis ultimately allows us to better understand
62 the seismic potential of the region.

63 **Keywords:** Malta Escarpment, seismic profile, sequential restoration, deformation rate.

64

65 1. Introduction

66 The restoration concept includes a wide range of methods (balanced cross-sections, back-stripping,
67 structural restoration etc.), which are applied to validate structural interpretations or to recover
68 deformation, subsidence or any other tectonic processes to be analysed. As seismic data are frequently
69 not associated with well data, application of sequential restoration techniques provides a powerful

70 tool for the validation of structural interpretation (Lopez-Mir et al 2014; Jamaludin et al., 2015;
71 Jitmahantakul et al., 2020), and formulation of kinematic structural models (Suppe, 1983; Suppe and
72 Medwedeff, 1990; Lopez-Mir et al., 2014). Restoration methods are usually based on ‘balanced cross
73 sections’ as defined by Dahlstrom (1969) and Elliot (1983), which are useful for prediction of
74 geometry at depth (Chamberlin 1910; Bally et al., 1966; Dahlstrom, 1969, 1970; White et al., 1986;
75 Williams and Vann, 1987; Groshong, 1990; Wang et al., 2017), and through which all available data
76 are analyzed to ensure that they are geometrically plausible and geologically consistent. These
77 methods usually follow reasonable assumptions about the pre-deformation setting and how rocks
78 behave during deformation in a given tectonic environment (Dahlstrom, 1969).

79 Since the pioneering studies of Bally et al. (1966) and Dahlstrom (1969), balanced cross sections
80 have been applied to section restoration for validation of structural interpretation and prediction of
81 geometry at depth in both contractional (Hossack, 1979; Boyer and Elliot, 1982; Suppe, 1983; Suppe
82 and Medwedeff, 1990) and extensional settings (Gibbs, 1983-1984; White et al., 1986, Williams and
83 Vann, 1987; Groshong, 1990). More recently, greater computational power has led to a significant
84 acceleration in section modelling and restorations (see Gratier et al., 1991; Egan et al., 1996; Maerten,
85 2007, among many others). Thanks to such a technological advance, structural balancing and horizon
86 flattening were applied to rectify seismic interpretation in extensional settings (Jamaludin et al., 2015)
87 or to validate 2D seismic interpretation and to calculate extension in various rift phases
88 (Jitmahantakul et al., 2020). Application of the above-mentioned methods represents a powerful
89 approach for basin analysis and for detailing how deformation evolves through time in various
90 tectonic contexts (extensional, compressional or composite).

91 In this study, sequential restoration methods (see Supplementary Material for description) were
92 applied to analyse the rate of deformation of the extensional Malta Escarpment (hereinafter MESC,
93 see Fig. 1) fault system. The MESC is a former passive margin in the Western Ionian Basin that was
94 reactivated by the Nubia-Eurasia plate convergence during Plio-Quaternary times (Casero et al.,
95 1984; Argnani and Bonazzi, 2005). The reactivation of MESC involved the proximal part of a narrow
96 sedimentary basin in the hanging-wall of the fault system, previously named the ‘turbidite valley’
97 (see Gutscher et al., 2016 and Fig.1c), and its recent deformation is expressed by a belt of East-
98 dipping extensional faults slicing across the lower slope of the MESC. Fault activity has led to the
99 development of significant fault-scarps on the seafloor (Bianca et al., 1999; Argnani and Bonazzi,
100 2002, 2005) that sometimes exceed heights of 60 m (see Gambino et al., 2021). Holocene slip rates
101 estimated by Gambino et al. (2021) for these faults appear atypical when compared with general
102 values recorded in similar tectonic regimes (Galadini and Galli, 2000; Pizzi et al., 2002; Musumeci
103 et al., 2014; Stemberk et al., 2019). Since fault slip rate is an essential parameter in seismotectonic

104 analysis, and considering that the MESC fault system is described by many authors as the seismogenic
105 source for large historical earthquakes in the area (Piatanesi and Tinti, 1998; Bianca et al., 1999;
106 Azzaro and Barbano, 2000; Argnani and Bonazzi, 2005; Argnani et al., 2012), we undertook a
107 sequential restoration work-flow to model the Plio-Quaternary deformation rate of the reactivated
108 northern sector of the MESC fault system. The aim of this work is twofold, a) to reassess fault activity
109 and associated extension and slip rates through-time, and b) to discriminate which kind of processes
110 operate to create basin deformation.

111 Sequential restoration was performed on a tectono-stratigraphic model developed from the
112 interpretation of two high-resolution seismic profiles that transversally cross the MESC (see Gambino
113 et al.; 2021; Gutscher et al., 2016). After time-to-depth conversion of the seismic profiles (see
114 Gambino et al., 2001), several restoration methods such as sediment unloading and decompaction,
115 isostatic adjustments, erosion restoration, structural restoration and unfolding of the horizons were
116 performed in order to create a geologically consistent sequential restoration (see Supplementary
117 Material). Accordingly, the present-day tectono-stratigraphic model was sequentially restored back
118 to the initial stage of deformation. This approach provides a more reliable estimation of the fault's
119 deformation rate overtime, with significant implications for the seismic hazard of the investigated
120 region.

121

122 **2. Geological Setting**

123 The 300 km-long Malta Escarpment is located about 20 km offshore Eastern Sicily and separates the
124 thinned/oceanic crust of the Western Ionian Basin from the continental crust of the Pelagian block
125 (Scandone et al., 1981; Fabbri et al., 1982; Casero et al., 1984, Fig.1a). It represents a rifting or
126 spreading-like extensional relict inherited from the Permian-Triassic opening of Neo-Tethys (Şengör,
127 1979), and the subsequent Mesozoic spreading stage (Ben-Avraham and Grasso, 1991; Catalano et
128 al., 2001). The MESC fault system was reactivated during Quaternary times (Hirn et al., 1997; Bianca
129 et al., 1999; Argnani and Bonazzi, 2005; Palano et al., 2012; Cultrera et al., 2015; Gambino et al.,
130 2021) and is considered one of the most likely sources of major destructive earthquakes in the area
131 over historical times (e.g. the 1169 and 1693 events), even though the actual localization of such
132 events is still controversial (Piatanesi and Tinti, 1998; Bianca et al., 1999; Azzaro and Barbano, 2000;
133 Argnani and Bonazzi, 2005; Argnani et al., 2012; Gambino et al., 2021). This establishes the MESC
134 system as a crucial tectonic feature for the understanding of both the geodynamics of the central
135 Mediterranean and the seismotectonics of the Western Ionian Basin and south-eastern Sicily.

136 To the East of the MESC, the Ionian Basin (Fig.1a) is interpreted by many authors as a remnant
137 of the Mesozoic Tethys Oceanic crust (Carminati and Doglioni, 2005; Frinzone et al., 2011; Gallais,

138 et al., 2011; Polonia et al., 2017; Speranza et al., 2012; Valenti, 2011), even though the actual nature
139 of the underlying geology is still debated (Dellong et al., 2018). NW-directed subduction of the Ionian
140 oceanic crust beneath the European plate resulted in the development of a large accretionary wedge
141 in the Ionian Sea (the Ionian accretionary wedge or Calabrian accretionary wedge, see Gallais et al.,
142 2012; Polonia et al., 2016). In contrast to the widespread contraction that affects the accretionary
143 wedge, a narrow sector at the western termination of the Ionian Basin (i.e. the turbidite valley, see
144 Gutscher et al., 2016 and Fig.1c for location) has not yet been overthrust by the compressional front
145 of the Ionian Accretionary wedge. Rather, Plio-Quaternary extension is preserved in the area, where
146 the narrow turbidite basin is deformed by a belt of extensional faults that nucleated at the foot of the
147 MESC (F1, F2 and F3 in Fig. 2a; Gambino et al., 2021). Part of this extensional system has been
148 previously reported in the literature (see Hirn et al., 1997; Bianca et al., 1999; Argnani and Bonazzi,
149 2005; Monaco and Tortorici, 2007; Meschis et al., 2020). The turbidite basin is confined between the
150 MESC to the West, and the compressional front of the Ionian accretionary wedge to the East (Fig.1b).
151 The latter is crosscut to the North by the NW-trending, dextral North Alfeo Fault (NAF in Fig.1b, see
152 Gutscher et al., 2016), which is also known in the literature as the Alfeo-Etna fault (AEF; Polonia et
153 al. 2016, 2017; Sgroi et al. 2021). The AEF accommodates the SE-ward shifting of the Calabria-
154 Peloritani block (Fig.1b), and separates the extensional basin from the contractional domain of the
155 Ionian accretionary wedge (Fig.1b). According to Polonia et al. (2016), the dextral AEF belt includes
156 the Mt. Etna volcano tectonic structures and segments of the MESC that accommodate the tensional
157 component of deformation associated with Africa–Eurasia relative motion.

158 Submarine canyons excavated in the MESC slope (Micallef et al., 2019, Fig.1c) reveal that the
159 turbidite basin has been filled by both sediments being discharged from the subaerial footwall-block
160 of the Malta Escarpment, and (mainly) the sediments coming from the North, as demonstrated by
161 wave patterns observed in the sedimentary succession within the turbidite basin (Gutscher et al.,
162 2016). Recently, high-resolution seismic surveys in the area (Gutscher et al., 2016) and accurate
163 tectono-stratigraphic interpretation (Gambino et al. 2021), have allowed the active deformation
164 pattern affecting the northernmost sector of the MESC to be redefined. It is characterized by the
165 occurrence of three main, E-dipping fault segments, showing a slight right-lateral component (F1, F2,
166 and F3 in Figs. 1c and 2) mainly distributed along the foot of the MESC bathymetric scarp. According
167 to Gambino et al. (2021), F1 consists of a ~45 km long, two-branched structure, oriented N345E, with
168 a fault surface dipping toward the ENE at ~45°; F2 is a N340E trending two-branched structure, ~35
169 km-long dipping at 50° toward the ENE; F3 is a 56 km-long segment with a N352E-oriented surface
170 dipping toward the east at 55°. Empirical scaling relationships point to their high seismic potential,
171 especially for F3. Further East, a narrow graben structure, associated with the main fault system, is

172 found to longitudinally deform the turbidite valley, displacing both the section of Quaternary
173 sediments and the seafloor itself (F4, F5 and minor faults in between; [Fig.2a](#)).

174

175 **3. Tectono-stratigraphic model**

176 *3.1. Seismic Stratigraphy*

177 The seismic stratigraphy, following [Gambino et al. \(2021\)](#), has been subdivided in four main seismic
178 units (Pre-MES, MES, PQ1, and PQ2) according to well-defined bounding stratigraphic
179 discontinuities (horizons S1, S2, S3 and, seafloor S4, see [Fig.2](#)). To better constrain the step-by-step
180 restoration through time, the PQ1 unit has been further subdivided in three sub-units (PQ1a, PQ1b,
181 and PQ1c) according to the detected S3a and S3b bounding unconformities ([Fig.2](#)). Since no borehole
182 data are available for the study area, lithologies and ages of the seismic units have been interpreted
183 according to the available literature (see [Gambino et al., 2021](#) and references therein) and summarized
184 in [Tab.1](#). The Pre-MES unit represents the backbone of the Malta Escarpment and has been
185 interpreted as Meso-Cenozoic limestones and marls with sporadic volcanic and/or mud intrusions
186 ([Scandone et al., 1981](#); [Catalano et al., 2001](#); [Barreca, 2014](#)). The MES unit has been interpreted as
187 the Messinian sequence based on its seismic characters (high-reflectivity of the top-reflector, see [Lofi](#)
188 [et al., 2011](#); [Camerlenghi et al., 2019](#); [Micallef et al., 2019](#) and reference therein) and on its internal
189 seismic facies ([Butler et al., 2015](#)). The PQ1 unit (including its subunits PQ1a, PQ1b, and PQ1c) has
190 been interpreted as a Pliocene sedimentary sequence since it correlates with coeval units described
191 by [Camerlenghi et al., \(2019\)](#) and [Micallef et al. \(2018\)](#). According to these authors, the PQ1 subunits
192 are interpreted as sequences of siltstone (shale) and silty-sandstones, calc-lutites and marls, while the
193 PQ2 unit is interpreted as a Quaternary sequence given its seismic character and stratigraphic position.
194 Moreover, its basal erosional surface, dated to 650 ka ([Camerlenghi et al., 2019](#)), suggests a
195 correlation with the Middle-late Pleistocene calcarenite sequence outcropping on-land ([Servizio](#)
196 [Geologico d'Italia, 2011](#)).

197 Lastly, the interpreted seismic profiles have been Time/Depth converted (as reported in [Gambino et](#)
198 [al., 2021](#)) using a velocity model ([Tab. 1](#)) from the literature (see also [Tab.1](#) in [Gambino et al., 2021](#)
199 and references therein).

200

201 *3.2. Deformation Pattern*

202 According to [Gambino et al. \(2021\)](#), reactivation of the MESC system is evidenced by an array of
203 seaward-dipping, NNW–SSE trending, extensional faults. The system extends offshore from Catania
204 (Northern termination) to Siracusa (Southern termination) with a total length of ~60 km ([Fig.1](#)). The

205 extensional belt includes three main faults (F1, F2, and F3) running close to the MESC lower slope,
206 with a 3.5 km-wide graben structure further to the East bounded by the F4 and F5 faults (Fig. 2a).
207 The F3 structure is the longest fault, reaching a length of ~ 56 km. The activity of the MESC faults
208 has produced a cumulative vertical displacement of the seafloor of about 130 m (see Tab. 2a and b).
209 The offset across faults generally increases with depth involving the entire Plio-Quaternary sequence
210 and the Messinian top reflector (S2, Fig. 2). The estimated rate of fault movement ranges from 0.1
211 mm/yr during the Pliocene to ~ 0.4 mm/yr during the Pleistocene, with an acceleration of the vertical
212 deformation rate up to 10 mm/yr in the Holocene, measured along the seafloor scarp of the F3 fault
213 (see Gambino et al., 2021). However, this value is probably overestimated and could be the result of
214 various factors affecting bathymetry (erosion, slope instability, etc.).

215 Farther to the east, the turbidite basin is bounded by a structural high (the so called ‘uplifted area’
216 of Argnani and Bonazzi, 2005, Fig. 2a). This has been interpreted as a recent positive flower structure
217 (probably rooted within Messinian unit) resulting from the propagation of the NW-SE trending
218 dextral NAF (see Gutscher et al., 2016 and Fig. 1 for location) or, alternatively, as a forced fold
219 produced by the diapiric uprising of mantle-derived serpentinite material (Polonia et al., 2017). The
220 structural culmination is deformed on its shallower portion by a set of high-angle recent and still
221 active faults (Fig. 2a), which have also been considered in the restoration process. The kinematics of
222 these faults is related to the dextral strike-slip nature of NAF (Figs. 1, 2a) that produces a cumulative
223 normal component observed in seismic sections (Cir-01 in Fig.2a).

224

225 4. Restoring the model

226 To back-deform the tectono-stratigraphic model (Fig. 2), a workflow encompassing several
227 restoration methods (i.e. unloading of top units, decompaction of underlying units, isostatic
228 adjustments, erosion restoration, structural restoration and unfolding of horizons), was adopted (see
229 supplementary material). Fault displacement parameters, i.e. throw and extension, have been
230 measured at each restoration cycle. The throw is considered to be the vertical component of the fault
231 offset, independent of the section direction with respect to the fault trend; the extension is considered
232 to be the horizontal component of the fault offset measured along the analysed section. Then,
233 cumulative throw (i.e., sum of the throw values of all faults within the section) and cumulative
234 extension (i.e., the restored horizontal component of each restoration cycle) were reported in Tab. 2a
235 (CIR-01 profile) and Tab. 2b (P607 profile).

236 4.1. Restoration of the CIR-01 profile

237 The workflow that was followed to restore the CIR-01 profile involved 48 sequential steps that have
238 included a preliminary tectono-stratigraphic interpretation and a time/depth conversion of seismic
239 units. The most representative steps are shown in Fig.4 where the interpreted CIR-01 profile has been
240 restored by applying the proposed restoration workflow (see supplementary material).

241 After seismic interpretation (Step-01) and time/depth conversion (Step-02), restoration started
242 from the present-day structural configuration (Step-03). At this stage, Block4 is deformed by a graben
243 related to the activity of the F4 and F5 opposite-dipping faults (see Fig. 2) and by other minor faults
244 developed in the uplifted area to the east (see Fig. 2 for details). The graben represents the latest
245 structure to have formed (Gambino et al 2021), since the bounding faults show a constant offset with
246 depth (from PQ1 downward). Indeed, F5 that forms the easternmost fault of the graben (Fig. 2a),
247 shows displacement increasing with depth, indicating its older activity. For this reason, F5 has been
248 restored by several steps that adopt a “simple shear method” (see supplementary material).

249 In Step-05, the graben has been back-deformed by means of structural restoration applied to both
250 F4 and the minor faults within the graben. In Step-06, the PQ2 unit is back-stripped and the lower
251 units de-compacted accordingly. In Step-07, erosion of PQ1c has been considered in the restoring
252 workflow. To gather information about the amount of eroded succession, the pattern of internal
253 reflectors within the PQ1c unit has been analysed. The seismo-stratigraphic sequences observed in
254 Block1 and Block4b can be considered as lacking erosion since no stratigraphic truncations have been
255 detected. Conversely, parts of the PQ1c are missing in Block2, Block3 and Block 4a (Fig.3a).
256 Accordingly, restoration of the S3 horizon (top of PQc1 unit) is performed by considering the eroded
257 stratigraphic portion and following the geometric pattern of the basal bed of PQ1c unit (the S3a
258 horizon, Fig. 3b). Along Block4a, patterns of internal reflectors indicate significant amounts of
259 erosion with the PQ1c unit locally being only a third of the original stratigraphic thickness. Along
260 Block3, the reflector pattern is difficult to observe due to the chaotic setting, and erosion has been
261 restored by considering the adjacent Blocks 2 and 4.

262 In Step-12, all the fault offsets are restored with respect to S3 horizon. The constant with depth
263 displacement of faults in the uplifted area (FU2, FU3, FU4, FU5 in Figs. 2a and 4) is restored in one
264 step after the structural restoration of the S3 horizon. This indicates that the onset of faulting occurred
265 after the deposition of the PQ1c unit. At this step, the cumulative extension accommodated by all the
266 faults is ~127 m. In Step-13, unfolding is applied to the S3 horizon. The result is shown in Figs. 3d2
267 and 4.

268 In Step-20, the PQ1c is unloaded and lower units de-compacted, while in Step-27, faults are
269 restored with respect to the S3b horizon and a total extension of ~205 m is achieved. In Step-29, all
270 units are unfolded with respect to the S3b horizon. As for Step-13 described above, an inclined and a

271 horizontal datum were adopted for lower-slope and basin units, respectively. It is worth noting that
272 unfolding of the units produced a decoupling (space in Fig. 4) between the lower-slope units (PQ1a,
273 PQ1b and MES) and the Pre-Mes unit. The space reflects the concept of ‘area conservation’
274 (Chamberlin, 1910) that is required for 2D restorations. We interpret this feature as being related to
275 accommodation of sediments due to progressive loading. This interpretation could also explain the
276 upward concavity in Step-03 of S3a, S3b, and S3 horizons located on the MESC lower-slope (Fig.
277 4). Alternatively, the decoupling should be the result of layer-parallel extension, which could have
278 produced volume loss due to an out-of-the-section trending deformation (Bahroudi et al., 2003).

279 In Step-35, the PQ1b unit is unloaded and lower units de-compacted, while in Step-42, faults are
280 restored with respect to the S3a horizon (top of PQ1a unit). Restoration of the F5 fault led to an
281 inconsistency on the undeformed S2 horizon, which resulted in it being higher in the hanging wall.
282 Even though negligible, such a discrepancy could be the result of an incorrect picking of the S2
283 horizon.

284

285 *4.2. Restoration of the P607 profile*

286 The workflow followed for the sequential restoration of the P607 profile involved 19 steps among
287 which the salient ones are shown in Fig. 5. After preparation (interpretation, time-to-depth conversion
288 etc., Steps-01-05) of the seismic profile, the PQ2 unit is unloaded and underlying units de-compacted
289 (Step-06). As for other steps, in the presence of growth strata (see PQ2 unit at Step-05, Fig. 5)
290 sediment unloading and decompaction of lower units follows the operation explained in Fig. 3c (see
291 also supplementary material). Accordingly, different loading on underlying units (located in the
292 footwall and hanging wall, respectively), due to regional and local load (i.e. increased near fault), are
293 unloaded separately.

294 In Step-08, faults are restored. It is worth noting that, contrary to the CIR-01 profile, no erosional
295 restoration has been performed to the PQ1c unit since the S3 horizon does not provide an indication
296 of the amount of eroded sequence. This is possibly due to a paraconformity that hides the erosional
297 nature of the S3 surface (Fig. 2b). This aspect led to an overestimation of F1 throw (see Fig.6 and
298 section 5).

299 Unfolding is applied in Step-09. As for the CIR-01 seismic line, an inclined datum was used to
300 unfold units formed on the lower-slope and a horizontal one to unfold units located in the adjacent
301 turbidite basin. In Block2, offset produced by the F2 fault on the S3b horizon (top of the PQ1b unit,
302 see Fig. 3b) is not consistent with the extensional kinematics of the fault, since the footwall is lower
303 than the hanging wall. Moreover, the S3b horizon in Block2 is bent downwards approaching the F2
304 fault. Since bending is observed neither in the upper nor in the lower horizons, it could be the result

305 of local erosion produced by slope instability. Hence, the S3a horizon has been restored (see below)
306 using the lower S3b horizon as a reference template.

307 In Step-10, erosion of PQ1b at block2 has been restored (see also Fig. 3b), while in Step-12, the
308 PQ1c unit is unloaded and underlying units de-compacted. Faults are restored in Step-13, and
309 unfolding is applied to the S3b horizon in Step-14. In step-15, the PQ1b unit is unloaded and lower
310 units de-compacted. It is notable that the F2 fault does not produce offset on lower units (PQ1a and
311 MES), suggesting that this fault nucleated after the deposition of the PQ1a unit. In Step-16, faults are
312 restored with respect to the S3a boundary, and in Step-17 unfolding is applied to the S3a horizon.
313 The PQ1a unit has been back-stripped and faults are restored with respect to the S2 horizon in Step-
314 19.

315

316 4.3. *Fault displacement parameters and rate of deformation*

317 The results of the sequential restoration of each seismic profile allowed the investigation of vertical
318 (throw) and horizontal (extension) components of offset experienced by all the faults in the studied
319 sector and their contribution to the overall deformation of the MESC fault system (cumulative throw
320 and restored extension in Tabs. 2a and b for the CIR-01 and the P607 profiles, respectively). For each
321 restoration step, vertical displacement of all faults has been measured (cumulative throw in Tab. 2)
322 and plotted for each displaced unit (Fig. 6). Fault displacement parameters from unrestored seismic
323 sections are also plotted for comparison (Fig. 6a-c). After the restoration process, the measured values
324 of fault throw along the CIR-01 (Fig. 6b) and the P607 (Fig. 6d) profiles show a flattened trend
325 compared to the unrestored sections, marking a significant reduction of the vertical offsets for each
326 displaced horizon. In the CIR-01 profile, a throw reduction is observed for the MESC faults and it
327 progressively increases further back in time. From the PQ1b unit (Middle Pliocene) to the present-
328 day, the MESC faults (F1, F2, and F3) show a relatively flat throw trend with a cumulative throw of
329 about 50 m for each considered horizon (~25 m for the F2 and F3 faults, and ~75 m for the F1
330 structure, see Tab. 2a and Fig. 6b). The same trend and reduction in offset are observed in the P607
331 profile except for the PQ1c unit that seems to have experienced up to 250 m of vertical displacement
332 (Fig. 6d). Since the erosional surface at the base of the PQ1c unit is not clearly detectable in the P607
333 profile, the throw affecting the PQ1c top-horizon (S3 discontinuity) has not been restored relating to
334 the eroded stratigraphic thickness. This limitation probably produced an overestimation of the throw
335 value for the PQ1c unit. Considering that a decrease of about one half of the throw affecting the PQ1c
336 unit was measured in the adjacent CIR-01 profile (Fig. 6b) after restoring the eroded sedimentary
337 thickness, a more reliable throw in the order of ~100 m is inferred for the PQ1c unit also along the
338 P607 profile (see dashed black line in Fig. 6d).

339 The revised values of fault throw were then used to evaluate the vertical movement of the MESC
340 faults over time (Fig. 7a). During the considered time interval, faults vertically deform the seismic
341 units at an average rate of 0.15 mm/yr (0.18 and 0.14 mm/yr for CIR-01 and P607 profiles
342 respectively, Tab. 3a-b and Fig.7a). The maximum throw-rate value (0.4 mm/yr in the CIR-01) is
343 observed at the Lower-upper-Pliocene transition. During the Upper Pliocene-Pleistocene, throw-rates
344 decrease and stabilize at 0.09 and 0.05 mm/yr for the P607 and CIR-01 profiles, respectively. To
345 discriminate and separate the contribution of the MESC faults to the overall basin deformation
346 (vertical and horizontal components, corresponding to cumulative throw and restored extension,
347 respectively), throw and extension of the MESC extensional system (sum of F1, F2, and F3
348 components indicated as MESC throw and MESC extension in Tab. 2) have been compared with the
349 total amount of the recovered basin extension (restored extension in Tab. 2) achieved by back-
350 deforming all the faults (Fig. 7b). At the undeformed stage (see step 48 in Fig. 4 and Messinian times
351 in Fig. 7b), restoration of all faults results in ~ 800 m of total horizontal extension and ~640 m of
352 cumulative throw. At this stage, the MESC faults contribute 33% (258 m) of total extension and 39%
353 (251 m) of the achieved cumulative throw (Tab. 3a). Both the vertical and horizontal component of
354 total deformation (blue and red solid lines in Fig. 7b) decrease toward the present-day, roughly
355 correlating with the trend of the deformation components of the MESC faults (see blue and red dashed
356 lines in Fig. 7b). This pattern suggests that in the older stage (MES-PQ1a transition), deformation
357 was rather distributed in most of the faults detected in the tectono-stratigraphic model. The prevalence
358 of the extensional horizontal component provides an insight on this incipient stage of deformation,
359 with a probable diffuse extensional strain across the entire investigated sector. In the mature stage
360 (i.e., moving towards the present-day), almost the entire deformation (i.e., the 97.48% of vertical
361 component, see Tab.3a), is accommodated by the MESC faults, indicating strain localization along
362 these tectonic structures.

363

364 5. Discussion

365 The restoration sequence proposed here aims to better constrain the tectonic rates of faults slicing
366 across the MESC by means of seismo-stratigraphic analysis and restoration modelling. The
367 identification of an erosively truncated unit (the PQ1c top reflector) within the investigated
368 sedimentary section provides additional issues both in applying the restoration workflow and on the
369 estimation of the vertical deformation rate affecting the investigated sector during the Quaternary.
370 Nevertheless, the analysis of the PQ1c/PQ2 erosive truncation (dated at 650 ka, see Camerlenghi et
371 al., 2019) along the CIR-01 profile (Fig.3a) provides an estimation of the amount of erosion
372 experienced by the PQ1c top-reflector (S3 horizon). The reconstruction of the eroded PQ1c unit

373 reveals that up to about one third of its original thickness was eroded (Fig. 3a top-right). The
374 maximum amount of erosion has been inferred at the depocenter of the turbidite basin (70 m, see
375 block 4a in Fig.3a). Such an estimation was not possible in the P607 profile because of the nature of
376 the para-conformity erosive truncation (see Fig. 2b). This issue produced an overestimation of the F1
377 throw (~250 m) affecting the PQ1c unit. However, according to the restored offset in the adjacent
378 CIR-01 profile, the overestimation was corrected making the fault-throw curve for the P607 (Fig. 6d)
379 consistent with the values of fault throw achieved in the CIR-01 seismic line (Fig.6b). Restoration of
380 the PQ1c original thickness requires a review of previously estimated vertical deformation of the
381 MESC faults during the Quaternary (see Gambino et al., 2021, and Tab. 2a). The F1 restored throw
382 results in about only half of the unrestored one (i.e., from 146.20 m to 69.23 m in the CIR-01 profile
383 see Tab. 2a). Throw along the F2 structure is instead reduced by about one third (from 33.74 to 20.36
384 m, see Tab. 2a). Negligible reduction in offset is observed for the F3 fault. The different offset
385 reduction along the MESC faults is in line with the higher erosion rate expected along the hanging
386 wall blocks.

387 Besides the F1 and the F3 tectonic structures, restoration of the F2 fault does not show vertical
388 displacement for the PQ1a and MES units along the P607 profile (red line in Fig. 6d) and for the
389 PQ1a unit along the CIR-01 profile (Fig. 6b). These data suggest that the F2 fault likely nucleated
390 after deposition of the PQ1a unit and hence it is later than the F1 and F3 structures (Lower Pliocene
391 - see Fig. 6d and Step-15 in Fig.5). Sequential restoration allows us to derive information on the fault
392 throw and extension experienced by the entire investigated sector during the considered time-interval.
393 In this context, a throw rate for the MESC faults is calculated considering the age of displaced surfaces
394 in both seismic profiles (Fig. 7a). Since no well data are available, the age of the stratigraphic
395 boundaries could be affected by uncertainties and, accordingly, a reliable estimation of the fault rate
396 becomes rather challenging. The S2 surface (MES top horizon) correlates with the upper Messinian
397 limit and represents the only horizon whose age is well known from literature (5.3 Ma, Camerlenghi
398 et al., 2019; Lofi et al., 2011; Micallef et al., 2019). The PQ1 sediment package is Pliocene in age
399 (see Gambino et al., 2021 and references therein) but uncertainties persist about the ages of its sub-
400 units. Following this limitation, we propose age ranges based on the units' stratigraphic positions (see
401 Tab. 1).

402 A comparison between the cumulative throw and restored extension (all faults in Cir-01 profile;
403 blue and red solid lines in Fig. 7b) and throw and extension of MESC faults (F1, F2 and F3; blue and
404 red dashed lines in Fig. 7b) provides an insight into how deformation was modulated through time.
405 Plotted values show that throw and extension produced by the activity of the MESC faults (F1, F2,
406 and F3) have comparable values for each restoration step, as expected when the mean dip-angle (45°)

407 of the faults is taken into account. Throw and extension values maintain roughly constant trends with
408 a slight decrease from the Upper Messinian to the present-day. Conversely, throw and extension
409 values related to the activity of all detected faults (cumulative throw and restored extension) show
410 high values during the Messinian-Lower Pliocene transition. This pattern suggests that in the early
411 stages, extensional deformation was diffuse and probably controlled by all faults. In this time span,
412 MESC faults contributed only ~39% of the total throw and ~33% of the total extension (see the
413 restoration Step-48 in [Tab.3a](#)). As deformation continued, cumulative throw and extension decreased
414 and, approaching the present day (PQ2 in [Fig. 7b](#) and [Tab. 3a](#)), the total throw affecting the area has
415 been largely accommodated by the MESC faults (97.48%). Moreover, in the early deformation stage
416 (from MES to PQ1b in [Fig. 7b](#)) restored extension (red solid line) is higher than the total vertical
417 throw (blue solid line) suggesting that horizontal extension was the main component of deformation.
418 Then, from PQ1b onwards, a change in the deformation style is observed with a predominant vertical
419 component. This evidence allowed us to infer that another deformation process, characterized by a
420 major extensional horizontal component, worked simultaneously with the faults' activity in the early
421 stage of deformation. This process is probably related to a diffuse extensional strain developed before
422 fault nucleation or, alternatively, to ductile deformation in the underlying MES unit. It has been
423 suggested that the nature of an underlying detachment layer (frictional or ductile) may play a
424 significant role in developing localised or diffuse faulting in the overlying sedimentary cover
425 ([Bahroudi et al., 2003](#)). In this view, the early diffuse deformation observed in [fig.7b](#) could be the
426 result of a ductile level in the Messinian unit; with the effect of the ductile level progressively
427 decreasing due to thickness reduction (possibly due to migration out of the section) and faulting
428 localising in to MESC faults.

429 In the final stage of the CIR-01 restoration (from Step-43 to Step-48 in [Fig. 4](#)), the S2 horizon
430 (and related MES unit) remained strongly bent along Block 4. Considering the hyaline nature of the
431 underlying MES unit and that no extensional fault can explain such a bending, the S2 curvature is
432 probably the result of ductile deformation. Lateral escape of the plastic evaporites driven by the
433 increased vertical load is invoked to explain the anomalous bending of the S2 horizon. Salt
434 deformation cannot be restored by means of classical restoration methods since salt typically assumes
435 three-dimensional escape directions and dissolution ([Rowan and Ratliff, 2012](#)). Moreover, it is
436 observed how salt migration due to sediment load may produce similar effects of local subsidence
437 and uplift ([Rojo et al., 2020](#)), which could explain the non-horizontal attitude of the S2 horizon.

438 Finally, even if it is not the main object of the work, some considerations can be drawn on the
439 seismogenic potential of the MESC faults: fault dimensions (e.g., for F3), compared to recurrence
440 time interval (see [Gambino et al., 2021](#)), are compatible with the magnitudes estimated for large

441 historical earthquakes in the area (e.g., the 1693 and 1169 events) although other seismic sources such
442 as the Alfeo-Etna Fault (Polonia et al., 2016) must be considered as well in the seismotectonic
443 framework of the Western Ionian Basin (see also Gutscher et al., 2016). It is also justified by the
444 acceleration in vertical deformation affecting the MESC faults during the Holocene. Recent
445 extensional reactivation of the MESC faults could be related to tensional component associated with
446 Africa–Eurasia relative motion (Palano et al., 2012) and mostly accommodated by the Alfeo-Etna
447 Fault system, resulting in rifting processes within the Western Lobe of the Calabrian Arc accretionary
448 wedge (see also Polonia et al., 2016).

449

450 **6. Conclusion**

451 Sequential restoration was applied to a tectono-stratigraphic model derived from the interpretation of
452 two high-resolution seismic profiles crossing the Malta Escarpment and the related extensional basin
453 offshore eastern Sicily. This allowed us to obtain reliable deformation rates for the investigated sector.
454 Sediment unloading/decompaction along with horizon unfolding, and erosional restoration have
455 proven powerful methods in re-interpretation/validation of previously interpreted seismic profiles,
456 and in assessing fault activity and the rate of crustal extension affecting the area.

457 The main outcomes stemming from this study are summarized as follows:

- 458 • Fault displacement parameters derived from the restored seismic profiles indicate that the
459 MESC faults maintain a roughly constant throw (about 150 m, see Fig. 7) for each restoration
460 step. Estimated rates of deformation suggest that the MESC faults throw-rates have been
461 modulated through time spanning from 0.09 to 0.40 mm/yr in the Pliocene, and from 0.05 to
462 0.09 mm/yr during the Pleistocene. Extensional rates are estimated at 0.06-0.31 mm/yr during
463 the Pliocene, and at 0.03-0.08 mm/yr during the Pleistocene.
- 464 • Throw and extension achieved from all faults in the CIR-01 profile indicate that during the
465 early stage (post-Messinian), a diffuse extensional strain affected the investigated sector. This
466 is evidenced by the significant difference between MESC faults deformation (i.e., MESC
467 extension and MESC throw in Fig. 7b) and the cumulative basin deformation (restored
468 cumulative extension and throw in Fig. 7b). In this context, the MESC faults contributed to a
469 third of total horizontal extension and throw during the early deformation stage (Lower
470 Pliocene). As deformation continued, the total deformation (restored cumulative extension
471 and throw in Fig. 7b) decreases and is taken up almost entirely by the MESC faults (Fig.7b).
472 At the present-day, MESC faults accommodate ~97.5% of the total vertical deformation as

473 well as most of the Quaternary extensional (horizontal) deformation affecting the investigated
474 sector.

- 475 • Data analysis also suggests that in the early stages of deformation (MES/PQ1a transition, [Fig.](#)
476 [7b](#)), the horizontal component of deformation prevailed over the vertical one. This suggest
477 that another process was active at that time along with the MESC faults, that were probably
478 still in their incipient stage. This extension may be related to ductile deformation within the
479 MES unit.
- 480 • Uncertainties persist about the present-day rate of deformation. The high rate of vertical
481 deformation affecting the MESC faults during the Holocene (3-7 mm/yr, see [Gambino et al.,](#)
482 [2021](#)), is in contrast with the relatively low fault deformation rate (up to 0.4 mm/yr) estimated
483 for the Pliocene sedimentary section. This would imply that a significant acceleration in the
484 (tectonic, non-tectonic?) deformation probably occurred along faults with strain localization
485 and reduction in frictional properties at fault cores.

486 In conclusion, structural interpretation and sequential restoration along the two analysed high-
487 resolution seismic profiles crossing the Malta Escarpment provide insights that allow us to assess
488 fault deformation rates along this tectonic belt, located in one of the most seismically hazardous areas
489 of the central Mediterranean. Back-deformation of a geologically constrained tectono-stratigraphic
490 model points to a revision of the throw-rates for the MESC faults. The vertical and horizontal
491 deformation rate calculated over time reveals that the investigated sector is a low deforming area. We
492 estimate a more reliable vertical offset that is about 2/3 of that measured in the unrestored sections
493 (e.g., Step-03 for the CIR-01 and Step-05 for the P607 profile, respectively) with significant
494 seismotectonic implications. The workflow presented here allows new insights into basin
495 deformation; in particular, two different processes, which contributed to the tectonic evolution of the
496 basin, have been quantitatively discriminated. Moreover, the workflow has shown itself to be a
497 powerful approach for analysis of basin deformation that can be applied to a wide range of tectonic
498 contexts (extensional, contractional or composite).

499

500 **References**

- 501 Airy, G. B. (1855). On the computation of the effect of the attraction of mountain-masses, as disturbing the
502 apparent astronomical latitude of stations of geodetic surveys. *Philosophical Transactions of the Royal*
503 *Society*, 145, 101–104.

- 504 Amato, A., Azzara, R., Basili, A., Chiarabba, C., Cocco, M., Di Bona, M. & Selvaggi, G. (1995). Main shock and
505 aftershocks of the December 13, 1990, Eastern Sicily earthquake. *Annali di Geofisica*, vol. 37 (2) p.255-
506 266.
- 507 Argnani, A., Armigliato, A., Pagnoni, G., Zaniboni, F., Tinti, S. & Bonazzi, C. (2012). Active tectonics along the
508 submarine slope of south-eastern Sicily and the source of the 11 January 1693 earthquake and tsunamis. *Nat.*
509 *Hazards Earth Syst. Sci.* 12 (5), 1311–1319. doi:10.5194/nhess-12-1311-2012.
- 510 Argnani, A., & Bonazzi, C. (2002). Tectonics of eastern Sicily offshore: preliminary results from the MESC 2001
511 marine seismic cruise. *Boll. Geofis. Teor. Appl.* 43 (3–4), 177–193
- 512 Argnani, A. & Bonazzi, C. (2005). Malta Escarpment fault zone offshore eastern Sicily: Pliocene-Quaternary
513 tectonic evolution based on new multichannel seismic data. *Tectonics* 24, TC4009.
514 doi:10.1029/2004TC001656.
- 515 Azzaro, R. & Barbano, M.S. (2000). Analysis of the seismicity of southeastern Sicily: a proposed tectonic
516 interpretation. *Ann. Geofisc.* 43 (1), 171–188. doi:10.4401/ag-3628.
- 517 Baldwin, B. & Butler, C.O. (1985). Compaction curves. *AAPG Bulletin*, 69 (4), 622-626.
- 518 Bahroudi A., Koyi, H.A. & Talbot, C.J. (2003). Effect of ductile and frictional décollements on style of extension.
519 *Journal of Structural Geology* 25, 1401 – 1423.
- 520 Bally, A. W., P. L. Gordy, and G. A. Stewart, 1966, Structure, seismic data, and orogenic evolution of southern
521 Canadian Rocky Mountains: *Bulletin of Canadian Petroleum Geology*, 14, 337–381.
- 522 Barnett, J.A.M., Mortimer, J., Rippon, J.H., Walsh, J.J. & Watterson, J. (1987). Displacement geometry in the
523 volume containing a single normal fault. *American Association of Petroleum Geologists Bulletin* 71 (8):
524 925-937.
- 525 Barreca, G. (2014). Geological and geophysical evidences for mud diapirism in south-eastern Sicily (Italy) and
526 geodynamic implications. *J. Geodyn.* 82, 168–177. doi:10.1016/j.jog.2014.02.003
- 527 Ben-Avraham, Z., and Grasso, M. (1991). Crustal structure variations and transcurrent faulting at the eastern and
528 western margins of the eastern Mediterranean. *Tectonophysics* 75, 269–277. doi:10.1016/0040-
529 1951(91)90326-N.
- 530 Bianca, M., Monaco, C., Tortorici, L. & Cernobori, L. (1999). Quaternary normal faulting in southeastern Sicily
531 (Italy): a seismic source for the 1693 large earthquake. *Geophys. J. Int.* 139, 370–394. doi:10.1046/j.1365-
532 246x.1999.00942.x
- 533 Boyer, S.E. & Elliot, D. (1982). Thrust systems. *Bullet. Am. Assoc. Petrol. Geol.* 66, 1196e1230.
- 534 Brewer, R. C. & Kenyon, P. M. (1996). Balancing Salt Dome Uplift and Withdrawal Basin Subsidence in Cross-
535 Section. *Journal of Structural Geology* 18 (4): 493-504. doi:10.1016/0191-8141(95)00098-X

- 536 Butler, R.W.H., Lickorish, W.H., Grasso, M., Pedley, H.M. & Ramberti, L. (1995). Tectonics and sequence
537 stratigraphy in Messinian basins, Sicily: Constraints on the initiation and termination of the Mediterranean
538 salinity crisis. *Geological Society of America Bulletin*, 107(4), 425-439. doi:10.1130/0016-
539 7606(1995)107<0425:TASSIM>2.3.CO;2
- 540 Butler, R.W.H., Maniscalco, R., Sturiale, G. & Grasso, M. (2015). Stratigraphic variations control deformation
541 patterns in evaporite basins: Messinian examples, onshore and offshore Sicily (Italy). *J. Geol. Soc.* 172,
542 113–124. doi:10.1144/jgs2014-024
- 543 Camerlenghi, A., Del Ben, A., Hübscher, C., Forlin, E., Geletti, R., Brancatelli, G., Micallef, A., Saule, M., &
544 Facchin, L. (2019). Seismic markers of the Messinian salinity crisis in the deep Ionian basin. *Basin*
545 *Research*, 32 (4), 716-738. doi:10.1111/bre.12392.
- 546 Carminati E. & Doglioni C. (2005): Mediterranean tectonics. In *Encyclopedia of Geology*, Elsevier, 135-146
- 547 Casero, P., Cita, M. B., Croce, M., and De Micheli, A. (1984). Tentativo di interpretazione evolutiva della Scarpata
548 di Malta basata sui dati geologici e geofisici. *Mem. Soc. Geol. It.* 27, 233–254.
- 549 Catalano, R., Doglioni, C. & Merlini, S. (2001). On the Mesozoic Ionian basin. *Geophysical Journal International*
550 144(1), 49-64. doi:10.1046/j.0956-540X.2000.01287.x
- 551 Catalano, R., Valenti, V., Albanese, C., Accaino, F., Sulli, A., Tinivella, U. et al. (2013). Sicily's fold-thrust belt
552 and slab roll-back: The SI.RI.PRO. seismic crustal transect. *Journal of the Geological Society* 170(3), 451-
553 464. doi:10.1144/jgs2012-099
- 554 Chamberlin, R.T., (1910). The Appalachian folds of central Pennsylvania. *The Journal of Geology* 18, 228-251.
- 555 Chamot-Rooke, N., Rangin, C. & Le Pichon, X. (2005). DOTMED–Deep Offshore Tectonics of the
556 Mediterranean: a synthesis of deep marine data in eastern Mediterranean. *Mémoire de la Société géologique*
557 *de France & American Association of Petroleum Geologists*. special number, 177: 64 pp, 9 maps with CD-
558 ROM.
- 559 Cultrera, F., Barreca, G., Scarfi, L. & Monaco, C. (2015). Fault reactivation by stress pattern reorganization in the
560 Hyblean foreland domain of SE Sicily (Italy) and seismotectonic implications. *Tectonophysics*, 661, 215-
561 228, doi: org/10.1016/j.tecto.2015.08.043.
- 562 D'Agostino, N., and Selvaggi, G. (2004). Crustal motion along the eurasia-nubia plate boundary in the calabrian
563 arc and sicily and active extension in the messina straits from GPS measurements. *J. Geophys. Res.* 109,
564 B11402. doi:10.1029/2004JB002998
- 565 Dahlstrom, C.D.A. (1969). Balanced cross sections. *Canadian Journal of Earth Sciences* 6, 743–757.
- 566 Dahlstrom, C.D.A., (1970). Balanced cross sections. *Can. J. Earth Sci.* 18, 332e406.

- 567 Dellong, D., Klingelhoefer, F., Kopp, H., Graindorge, D., Margheriti, L., Moretti, M. et al. (2018). Crustal structure
568 of the Ionian basin and eastern Sicily margin: Results from a wide-angle seismic survey. *Journal of*
569 *Geophysical Research: Solid Earth*, 123, 2090–2114. <https://doi.org/10.1002/2017JB015312>
- 570 Dickinson, G. (1953). Geological aspects of abnormal reservoir pressures in Gulf Coast, Louisiana: AAPG
571 *Bulletin*, v. 37, p. 410–432.
- 572 Egan, S. S., Buddin, T. S., Kane, S. J., and Williams, G. D., (1997). Three-dimensional modelling and visualization
573 in structural geology: new techniques for the restoration and balancing of volumes, In: *Proceedings of the*
574 *1996 Geoscience Information Group Conference on Geological Visualisation: Electronic Geology*, V. 1,
575 *Paper 7*, p.67-82.
- 576 Egan, S.S., Buddin, T.S., Kane, S.J. & Williams G.D. (1996). Three-dimensional modeling and visualization in
577 structural geology: new techniques for the restoration and balancing of volumes. In: *Proceedings of the 1996*
578 *Geoscience Information Group Conference on Geological Visualization, Electronic Geology 1*, pp. 67–82.
579 *Paper 7*.
- 580 Elliott, D. (1983). The construction of balanced cross sections. *Journal of Structural Geology* 5, 101.
- 581 Fabbri, A., Rossi, S., Sartori, R., and Barone, A. (1982). Evoluzione neogenica dei margini marini dell'Arco
582 Calabro-Peloritano: implicazioni geodinamiche. *Mem. Soc. Geol. It.* 24, 357–366.
- 583 Frizon de Lamotte, D., Raulin, C., Mouchot, N., Wrobel-Daveau, J.C., Blanpied, C. & Ringenbach J.C. (2011).
584 The southernmost margin of the Tethys realm during the Mesozoic and Cenozoic: Initial geometry and
585 timing of the inversion processes. *Tectonics* 30, TC3002, doi:10.1029/2010TC002691.
- 586 Galadini, F. & Galli, P. (2000). Active tectonics in the central Apennines (Italy) - input data for seismic hazard
587 assessment. *Natural Hazards*, 22(3), 225-268. doi:10.1023/A:1008149531980
- 588 Gallais, F., Gutscher, M.A., Graindorge, D., Chamot-Rooke, N. & Klaeschen, D. (2011). A Miocene tectonic
589 inversion in the Ionian Sea (central Mediterranean): evidence from multichannel seismic data. *J. Geophys.*
590 *Res.* 116, B12108. doi:10.1029/2011JB008505
- 591 Gallais, F., Gutscher, M.A, Klaeschen, D. & Graindorge. D. (2012). Two-Stage Growth of the Calabrian
592 Accretionary Wedge in the Ionian Sea (Central Mediterranean): Constraints from Depth-Migrated
593 Multichannel Seismic Data. *Marine Geology* 326-328: 28-45. doi:10.1016/j.margeo.2012.08.006
- 594 Gambino, S., Barreca G., Gross F., Monaco C., Krastel, S. & Gutscher, MA (2021). Deformation Pattern of the
595 Northern Sector of the Malta Escarpment (Offshore SE Sicily, Italy): Fault Dimension, Slip Prediction, and
596 Seismotectonic Implications. *Front. Earth Sci.* 8:594176. doi: 10.3389/feart.2020.594176
- 597 Ge, H., Jackson, M.P. & Vendeville, B.C. (1997). Kinematics and dynamics of salt tectonics driven by
598 progradation: AAPG *Bulletin* 81, 398–423.
- 599 Gibbs, A.D. (1983). Balanced cross-section construction from seismic sections in areas of extensional tectonics.
600 *Journal of Structural Geology* 5, 153–160.

601 Gibbs, A.D. (1984). Structural evolution of extensional basin margins. *Journal of the Geological Society, London*
602 141, 609–620.

603 Gratier, J.P., Guillier, B., Delorme, A. & Odonne, F. (1991). Restoration and balance of a folded and faulted surface
604 by best-fitting of finite elements: principle and applications. *Journal of Structural Geology* 13, 111–115.

605 Grenerczy, G., Sella, G., Stein, S., and Kenyeres, A. (2005). Tectonic implications of the GPS velocity field in the
606 northern Adriatic region. *Geophys. Res. Lett.* 32, L16311. doi:10.1029/2005GL022947

607 Groshong Jr., R.H. (1990). Unique determination of normal fault shape from hangingwall bed geometry in
608 detached half grabens. *Eclogae Geol. Helvetiae* 83, 455e471.

609 Groshong Jr., R.H., Bond, C.E., Gibbs, A., Ratcliff, R. & Wiltchko, D. (2012). Preface: structural balancing at
610 the start of the 21st century: 100 years since Cham-Berlin. *J. Struct. Geol.* 41, 1e5.

611 Gross, F., Krastel, S., Geersen, J., Hinrich, B.J., Ridente, D., Chiocci, F. L. et al. (2016). The limits of seaward
612 spreading and slope instability at the continental margin offshore Mt. Etna, imaged by high-resolution 2D
613 seismic data. *Tectonophysics* 667, 63–76. doi:10.1016/j.tecto.2015.11.011

614 Gutscher, M.-A., Dominguez, S., Mercier de Lepinay, B., Pinheiro, L., Gallais, F., Babonneau, N., et al. (2016).
615 Tectonic expression of an active slab tear from high-resolution seismic and bathymetric data offshore Sicily
616 (Ionian Sea). *Tectonics* 35, 39–54. doi:10.1002/2015TC003898

617 Gutscher, M.-A., Kopp, H., Krastel, S., Bohrmann, G., Garlan, T., Zaragosi, S., et al. (2017). Active tectonics of
618 the Calabrian subduction revealed by new multibeam bathymetric data and high-resolution seismic profiles
619 in the Ionian Sea (Central Mediterranean). *Earth Planet Sci. Lett.* 461, 61–72.
620 doi:10.1016/j.epsl.2016.12.020

621 Hirn, A., Nicolich, R., Gallart, J. and the ETNASEIS scientific Group (1997). Roots of Etna Volcano, faults of
622 great earthquakes. *Earth and Planetary Science Lett.* 148, 171-191.

623 Hossack, J.R. (1979). The use of balanced cross sections in the calculation of orogenic contraction: a review. *J.*
624 *Geol. Soc. Lond.* 136, 705e711.

625 Jackson, M.P.A., & Talbot, C. J. (1991). *A glossary of salt tectonics*: Bureau of Economic Geology. Austin, TX:
626 University of Texas at Austin.

627 Jamaludin, S. N. F., Latiff, A. H. A., & Ghosh, D. P. (2015). Structural balancing vs horizon flattening on seismic
628 data: Example from extensional tectonic setting. Paper presented at the IOP Conference Series: Earth and
629 Environmental Science, , 23(1) doi:10.1088/1755-1315/23/1/012003

630 Jitmahantakul, S., Phetheet, J., & Kanjanapayont, P. (2020). 2D sequential restoration and basin evolution of the
631 wichianburi sub-basin, phetchabun basin, central thailand. *Frontiers in Earth Science*, 8
632 doi:10.3389/feart.2020.578218

- 633 Kokinou, E., Vafidis, A., Loucogiannakis, M. & Louis, I. (2013). Deep seismic imaging and velocity estimation
634 in Ionian Sea. *J. Balkan Geophys. Soc.* 6 (2), 100–116.
- 635 Laurent, G., Caumon, G., Bouziat, A., & Jessell, M. (2013). A parametric method to model 3D displacements
636 around faults with volumetric vector fields. *Tectonophysics* 590, pp.83-93. [ff10.1016/j.tecto.2013.01.015](https://doi.org/10.1016/j.tecto.2013.01.015)
637 [ffhal-01301478](https://hal.archives-ouvertes.fr/hal-01301478)
- 638 Le Meur, D. (1997). Etude géophysique de la structure profonde et de la tectonique active de la partie occidentale
639 de la Ride Méditerranéenne [Ph.D. thesis]. Paris (FR): University of Paris XI.
- 640 Lofi, J., Deverchère, J., Gaullier, V., Gillet, H., Gorini, C., Guennoc, P., et al. (2011). Seismic atlas of the messinian
641 salinity crisis markers in the mediterranean and black seas. *Mém. Soc. Géol. CCGM* 179, 1–72.
- 642 Lopez-Mir, B., Anton Muñoz, J., & García Senz, J. (2014). Restoration of basins driven by extension and salt
643 tectonics: Example from the cotiella basin in the central pyrenees. *Journal of Structural Geology*, 69(PA),
644 147-162. [doi:10.1016/j.jsg.2014.09.022](https://doi.org/10.1016/j.jsg.2014.09.022)
- 645 Maerten, L., 2007. Geomechanics to solve structure related issues in petroleum reservoirs. *AAPG Eur. Reg. Newsl.*
646 2, 2-3.
- 647 Maesano, F.E., Tiberti, M.M. & Basili, R. (2017). The Calabrian Arc: three-dimensional modelling of the
648 subduction interface. *Sci. Rep.* 7, 8887. [doi:10.1038/s41598-017-09074-8](https://doi.org/10.1038/s41598-017-09074-8)
- 649 Meschis, M., Scicchitano, G., Roberts, G. P., Robertson, J., Barreca, G., Monaco, C., et al., (2020). Regional
650 deformation and offshore crustal local faulting as combined processes to explain uplift through time
651 constrained by investigating differentially uplifted late quaternary paleoshorelines: The foreland hyblean
652 plateau, SE sicily. *Tectonics*, 39(12) [doi:10.1029/2020TC006187](https://doi.org/10.1029/2020TC006187)
- 653 Milia, A., & Torrente, M. M. (2018). Extensional Messinian basins in the Central Mediterranean (Calabria, Italy):
654 new stratigraphic and tectonic insights. *Oil & Gas Science and Technology – Revue d’IFP Energies*
655 *nouvelles*, Institut Français du Pétrole 73, pp.45. [10.2516/ogst/2018040](https://doi.org/10.2516/ogst/2018040). [hal-01902842](https://hal.archives-ouvertes.fr/hal-01902842)
- 656 Micallef, A., Camerlenghi, A., Garcia-Castellanos, D., Cunarro Otero, D., Gutscher, M.-A., Barreca, G., et al.,
657 (2018). Evidence of the zanclean megaflood in the eastern mediterranean basin. *Scientific Reports*, 8(1)
658 [doi:10.1038/s41598-018-19446-3](https://doi.org/10.1038/s41598-018-19446-3)
- 659 Micallef, A., Camerlenghi, A., Georgiopoulou, A., Garcia-Castellanos, D., Gutscher, M.-A., Lo Iacono, C., et al.
660 (2019). Geomorphic evolution of the Malta Escarpment and implications for the Messinian evaporative
661 drawdown in the eastern Mediterranean Sea. *Geomorphology* 327, 264–283.
662 [doi:10.1016/j.geomorph.2018.11.012](https://doi.org/10.1016/j.geomorph.2018.11.012)
- 663 Minelli, L. & Facenna, C. (2010). Evolution of the Calabrian Accretionary wedge (Central Mediterranean).
664 *Tectonics* 29 (4), 1-21. <http://dx.doi.org/10.1029/2009TC002562>
- 665 Monaco, C. & Tortorici, L. (2007). Active faulting and related tsunamis in eastern Sicily and south-western
666 Calabria. *Bollettino di Geofisica Teorica e Applicata* 48 (2), 163-184.

- 667 Mastrolembo, V. B., Serpelloni, E., Argnani, A., Bonforte, A., Bürgmann, R., Anzidei, M. P., et al. (2014). Fast
668 geodetic strain-rates in eastern sicily (southern Italy): new insights into block tectonics and seismic potential
669 in the area of the great 1693 earthquake. *Earth Planet Sci. Lett.* 404, 77–88. doi:10.1016/j.epsl.2014.07.025
- 670 Musumeci, C., Scarfi, L., Palano, M. & Patanè., D. (2014). Foreland Segmentation Along an Active Convergent
671 Margin: New Constraints in Southeastern Sicily (Italy) from Seismic and Geodetic
672 Observations. *Tectonophysics* 630 (C), 137-149. doi:10.1016/j.tecto.2014.05.017
- 673 Nixon, C.W., Sanderson, D.J., Dee, S.J., Bull, J.M., Humphreys, R.J. & Swanson, M.H. (2014). Fault interactions
674 and reactivation within a normal-fault network at Milne point, Alaska. *AAPG Bulletin* 98 (10), 2081-2107.
675 doi:10.1306/04301413177
- 676 Palano, M., Ferranti, L., Monaco, C., Mattia, M., Aloisi, M., Bruno, V., Cannavò, F.& Siligato, G. (2012). GPS
677 velocity and strain fields in Sicily and southern Calabria, Italy: updated geodetic constraints on tectonic
678 block interaction in the central Mediterranean. *J. Geophys. Res.* 117, B07401.
679 <http://dx.doi.org/10.1029/2012JB009254>
- 680 Peel, F.J. (2014a). The Engines of Gravity-Driven Movement on Passive Margins: Quantifying the Relative
681 Contribution of Spreading Vs. Gravity Sliding Mechanisms. *Tectonophysics* 633 (1), 126-142.
682 doi:10.1016/j.tecto.2014.06.023.
- 683 Peel, F.J. (2014b). How do Salt Withdrawal Minibasins Form? Insights from Forward Modelling, and Implications
684 for Hydrocarbon Migration. *Tectonophysics* 630 (C), 222-235. doi:10.1016/j.tecto.2014.05.027.
- 685 Piatanesi, A. & Tinti, S. (1998). A revision of the 1693 eastern Sicily earthquake and tsunami. *J. Geophys. Res.*
686 *Solid Earth* 103 (B2), 2749–2758. doi:10.1029/97JB03403.
- 687 Pizzi, A., Calamita, F., Coltorti, M. & Pieruccini, P. (2002). Quaternary normal faults, intramontane basins and
688 seismicity in the umbria-marche-abruzzesi apennine ridge (italy): Contribution of neotectonic analysis to
689 seismic hazard assessment. *Bollettino Societa Geologica Italiana* 1(2), 923-929.
- 690 Polonia, A., Torelli, L., Artoni, A., Carlini, M., Faccenna, C., Ferranti, L., et al. (2016). The Ionian and Alfeo-Etna
691 fault zones: New segments of an evolving plate boundary in the central Mediterranean sea? *Tectonophysics*
692 675, 69-90. doi:10.1016/j.tecto.2016.03.016
- 693 Polonia, A., Torelli, L., Gasperini, L., Cocchi, L., Muccini, F., Bonatti, E. et al. (2017). Lower plate serpentinite
694 diapirism in the Calabrian arc subduction complex. *Nature Communications*, 8(1). doi:10.1038/s41467-017-
695 02273-x
- 696 Rojo, L.A., Koyi, H., Cardozo, N. & Escalona, A. (2020). Salt tectonics in salt-bearing rift basins: Progradational
697 loading vs extension. *Journal of Structural Geology* 141 doi:10.1016/j.jsg.2020.104193
- 698 Rowan & Ratliff (2012). Cross-section restoration of salt-related deformation: Best practices and potential pitfalls.
699 *J. Structural Geol.* 41, 24-37.

- 700 Scandone, P., Patacca, E., Radoicic, R., Ryan, W. B. F., Cita, M. B., Rawson, M., et al. (1981). Mesozoic and
701 cenozoic rocks from Malta escarpment (Central Mediterranean). *AAPG Bull.* 65 (7), 1299–1319.
702 doi:10.1306/03B5949F-16D1-11D7-8645000102C1865D.
- 703 Schultz-Ela, D.D. (1992). Restoration of cross-sections to constrain deformation processes of extensional terranes.
704 *Mar. Petrol. Geol.* 9, 372e388.
- 705 Sclater, J.G., & Christie, P.A. (1980). Continental stretching: An explanation of the post-Mid-Cretaceous
706 subsidence of the central North Sea Basin. *J. Geophysical Res. Solid Earth* 85 (B7), 3711-3739.
- 707 Şengör, A. M. C. (1979). Mid-mesozoic closure of permo-triassic tethys and its implications. *Nature* 279, 590-
708 593. doi:10.1038/279590a0
- 709 Servizio Geologico d'Italia (2011). Foglio 641 Augusta della Carta Geologica d'Italia alla scala 1:50.000.
710 Coordinatore scientifico Carbone S. Direttore dei rilevamenti Lentini F. Note illustrative a cura di Carbone
711 S. (ISPRA). 247.
- 712 Sgroi, T., Polonia, A., Barberi, G., Billi, A., & Gasperini, L. (2021). New seismological data from the calabrian
713 arc reveal arc-orthogonal extension across the subduction zone. *Scientific Reports*, 11(1)
714 doi:10.1038/s41598-020-79719-8.
- 715 Speranza, F., Minelli, L., Pignatelli, A., & Chiappini, M. (2012). The ionian sea: The oldest in situ ocean fragment
716 of the world? *Journal of Geophysical Research B: Solid Earth*, 117(12) doi:10.1029/2012JB009475.
- 717 Stemberk, J., Moro, G.D., Stemberk, J., Blahůt, J., Coubal, M., Košťák, B. et al. (2019). Strain monitoring of active
718 faults in the central apennines (italy) during the period 2002–2017. *Tectonophysics* 750 22-35.
719 doi:10.1016/j.tecto.2018.10.033
- 720 Suppe, J. (1983). Geometry and kinematics of fault-bend folding. *Am. J. Sci.* 283, 684e721.
- 721 Suppe, J., & Medwedeff, D. A. (1990). Geometry and kinematics of fault-propagation folding. *Eclogae Geologicae*
722 *Helveticae*, 83(3), 409-454.
- 723 Valenti, V. (2011). New insights from recently migrated CROP multichannel seismic data at the outermost
724 calabrian arc accretionary wedge (ionian sea). *Italian Journal of Geosciences*, 130(3), 330-342.
725 doi:10.3301/IJG.2011.05
- 726 Wang, W., Yin, H., Jia, D., Wu, Z., Wu, C. & Zhou, P. (2017). Calculating detachment depth and dip angle in
727 sedimentary wedges using the area–depth graph. *J. Struct. Geol.* <https://doi.org/10.1016/j.jsg.2017.11.014>.
- 728 Ward, S. (1994). Constraints on the seismotectonics of the central Mediterranean from very long baseline
729 interferometry. *Geophys. J. Int.* 117, 441–452. doi:10.1111/j.1365-246X.1994.tb03943.x White, N.J.,
730 Jackson, J.A., & McKenzie, D.P. (1986). The relationship between the geometry of normal faults and that
731 of sedimentary layers in their hanging walls. *J. Struct. Geol.* 8, 897e910.

732 Williams, G., Vann, I., (1987). The geometry of listric normal faults and deformation in their hanging walls. *J.*
733 *Struct. Geol.* 9, 789e795.

734

735 **Figure captions**

736 **Fig. 1** - a) Simplified tectonic setting of Sicily and the Western Ionian Basin. HP= Hyblean Plateau;
737 MESC= Malta Escarpment; SFTB= Sicilian Fold and Thrust Belt; CAW=Calabrian Accretionary
738 Wedge. Large blue arrows indicate diverging geodetic velocities (see Ward 1994; Mastrolembo et
739 al., 2014; D'Agostino and Selvaggi, 2004; Grenerczy et al., 2005; Palano et al., 2012) measured in
740 the foreland domain (Hyblean Plateau and Apulia Block) b) Main tectonic structures in the study area
741 with the F1, F2, and F3 faults representing the focus of this work. c) Location of 'turbidite valley'
742 and the analyzed seismic profiles (blue lines). Solid blue lines are the CIR-01 and P607 seismic
743 profiles discussed in the text.

744 **Fig. 2** - Tectono-stratigraphic models used for sequential restoration. a) CIR-01 profile with
745 identification of three main sectors: MESC slope, turbidite basin and uplifted area. The uplifted area
746 corresponds to the North Alfeo Fault system (NAF; [Gutscher et al., 2016](#)). b) P607 profile with the
747 MESC slope turbidite basin. For both profiles, the schematic block model (not to scale) used for the
748 restoration process is shown.

749 **Fig. 3** – Main restoration steps. a) Restoration of erosion of the PQ1c unit (CIR-01 profile). Internal
750 reflectors of Block 4b have been considered as the complete seismo-stratigraphic sequence.
751 Accordingly, missing reflectors of Blocks 2, 3 and 4a provide an indication of the amount of erosion.
752 b) Restoration of erosion of the PQ1b unit (P607 profile). S3b horizon (top of PQ1b) shows local
753 erosion (due to slope instability) highlighted by footwall/hangingwall offset. Restoration has been
754 performed using the lower unit top reflector (S3a horizon) as a template. c) Unloading of the upper
755 unit and decompaction of underlying ones. For units showing across-fault thickness variation
756 (growth-strata) we considered a regional load acting on both the footwall and hangingwall of the
757 considered fault, and a local load acting only on the hangingwall. As a result, different decompactions
758 of lower units is applied to the footwall and hangingwall. d) Unfolding of seismic units. Two data
759 have been considered since no paleo-bathymetric datum is available. Datum 2 (which is horizontal in
760 the turbidite basin and inclined on the slope) has been chosen since it is geologically reliable (see text
761 for description).

762 **Fig. 4** – Restoration sequence of CIR-01 profile. Bottom-right represents the present-day setting. In
763 every restoration cycle, structural restoration is performed, and the related amount of extension is
764 reported. At the end of each cycle, the inferred age is reported.

765 **Fig. 5** – Restoration sequence of the P607 profile. The present-day setting is shown in the bottom-
766 right. In every restoration cycle, structural restoration is performed, and the related amount of
767 extension is reported. At the end of each cycle, the inferred age is reported.

768 **Fig. 6** – Throw values measured on tectono-stratigraphic models before (a, c) and after (b, d)
769 restoration. In the time range axis, the measured units are reported. For the restored diagrams (b, d)
770 throw values are measured before the structural restoration steps. When the considered unit represents
771 the top unit of the sequence, the relative step numbers (related to [Figs. 4 and 5](#)) are reported above.

772 **Fig. 7** - a) Cumulative throw-rate of F1, F2 and F3 faults (MESC faults) relative to CIR-01 (blue line)
773 and P607 (red line). Every value is relative to the time interval between the seismic units reported

774 (inferred ages are reported in **Tab.1b**). Displacement components achieved from the restoration of the
 775 CIR-01 profile. Dotted lines are relative to MESC faults parameters (throw and extension respectively
 776 blue and red) and solid lines are relative to the cumulative parameters (throw and extension
 777 respectively blue and red) of all faults within the seismic profile.

778 **Tab. 1** – Physical parameters attributed to the detected seismic units used for sequential restoration.
 779 Ages, lithologies and seismic velocities are based on literature data (see [Gambino et al., 2021](#) and
 780 reference therein).

781 **Tab. 2** – Results achieved by means of the sequential restoration process (blue highlighted values
 782 are post-calculated). a) Data related to the restoration of the CIR-01 profile; b) Data related to the
 783 restoration of the P607 profile.

784 **Tab. 3** – Main results of sequential restoration (values of throw and extension) and data elaboration
 785 (rates) of CIR-01 (a) and P607 (b).

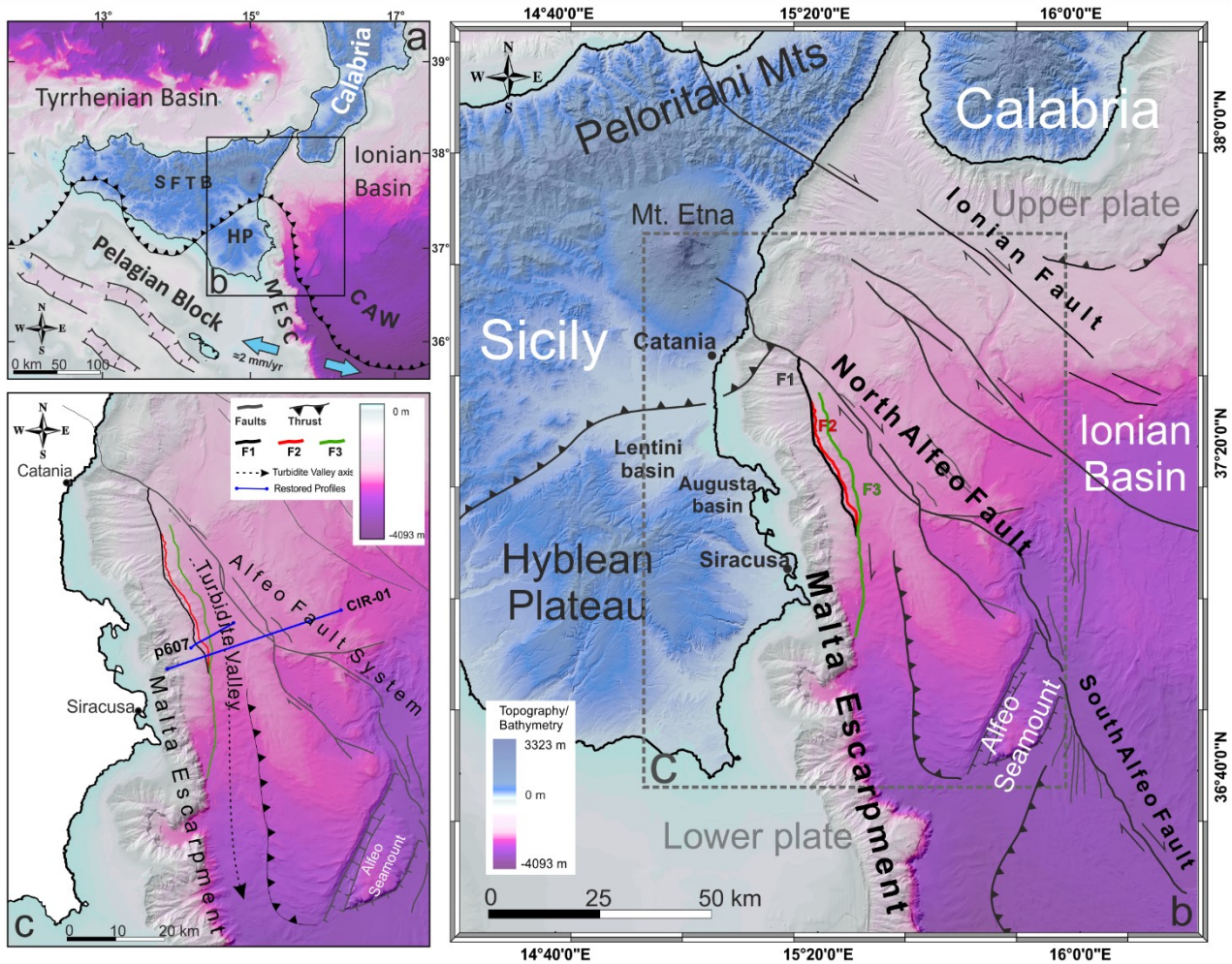


Fig.1

786
 787
 788

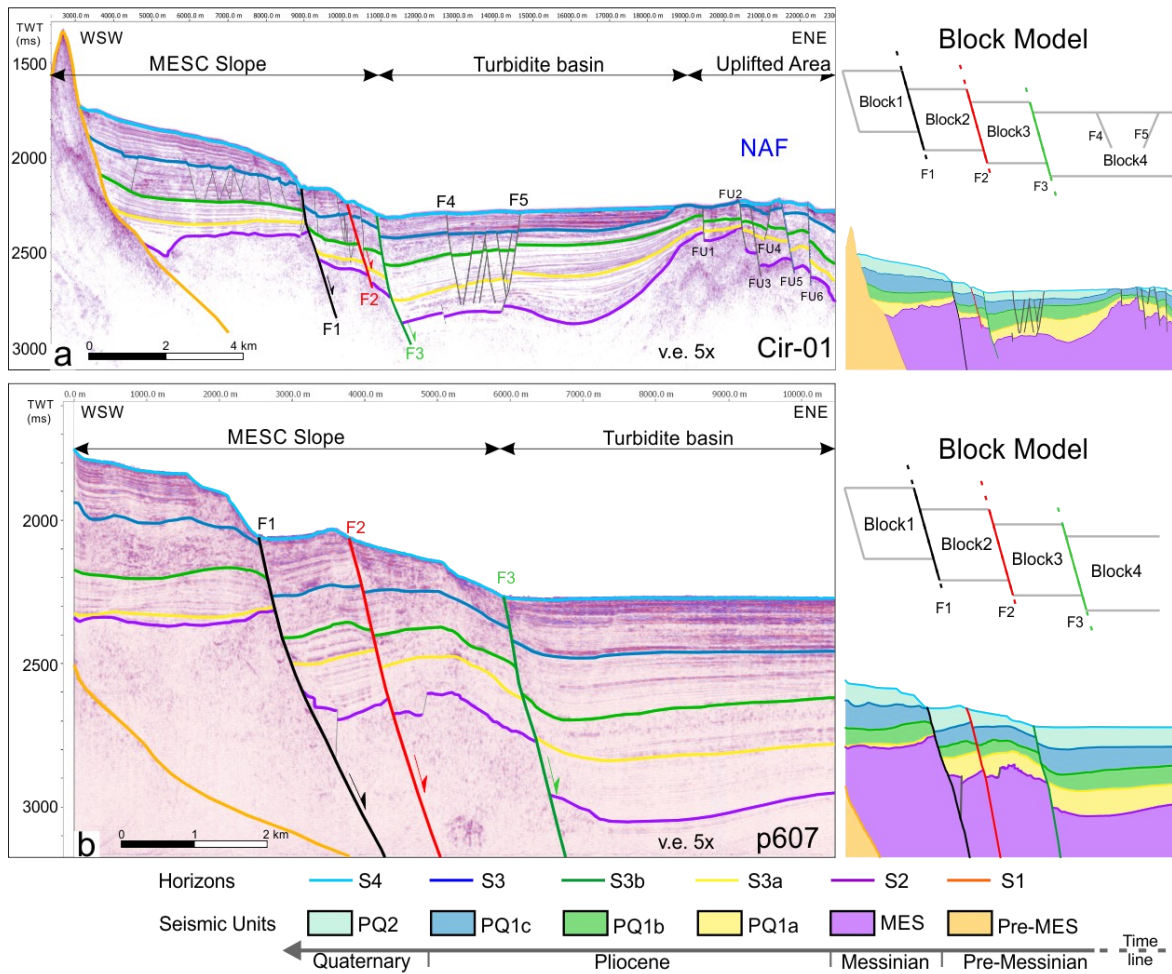


Fig.2

789
790
791

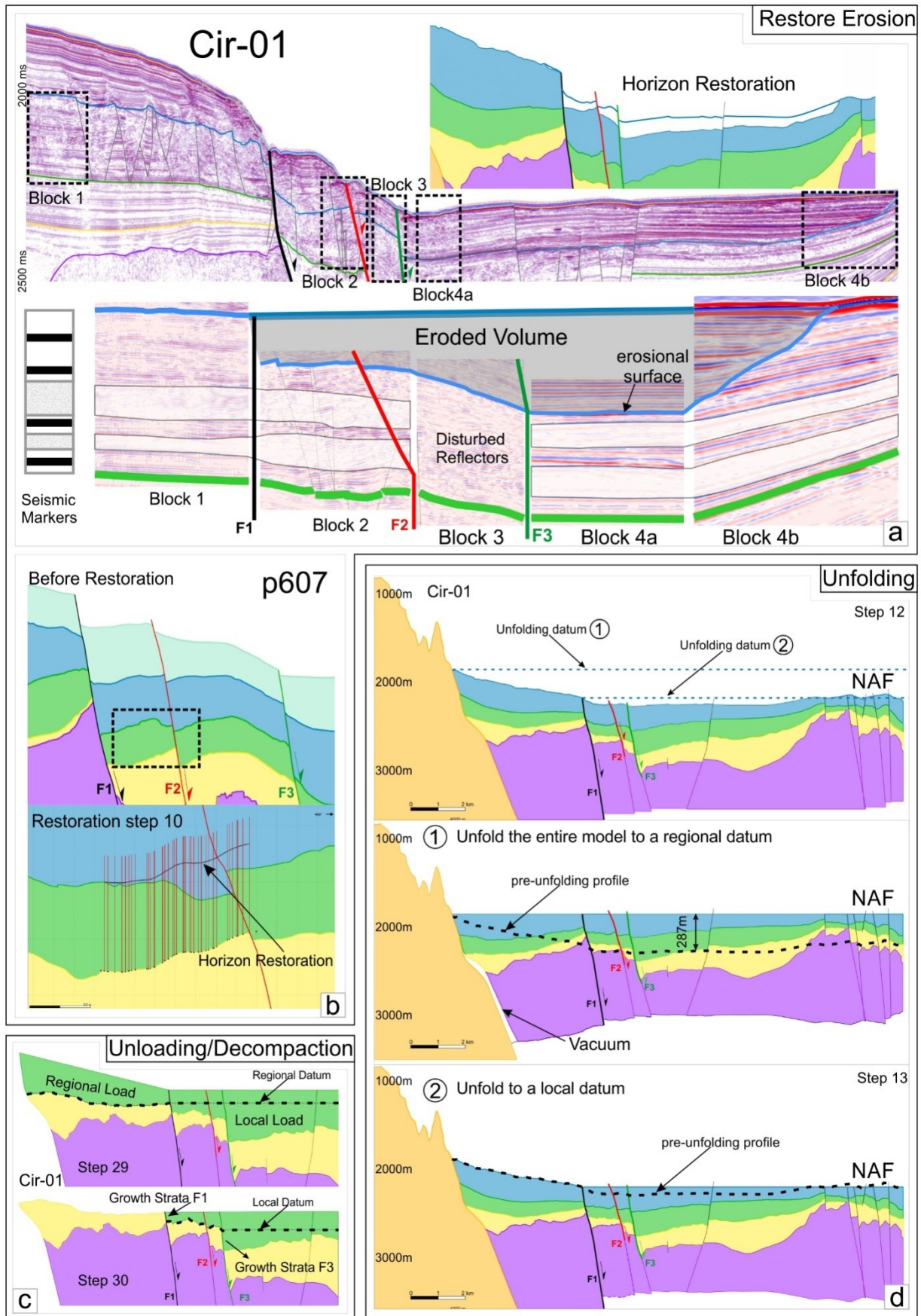


Fig.3

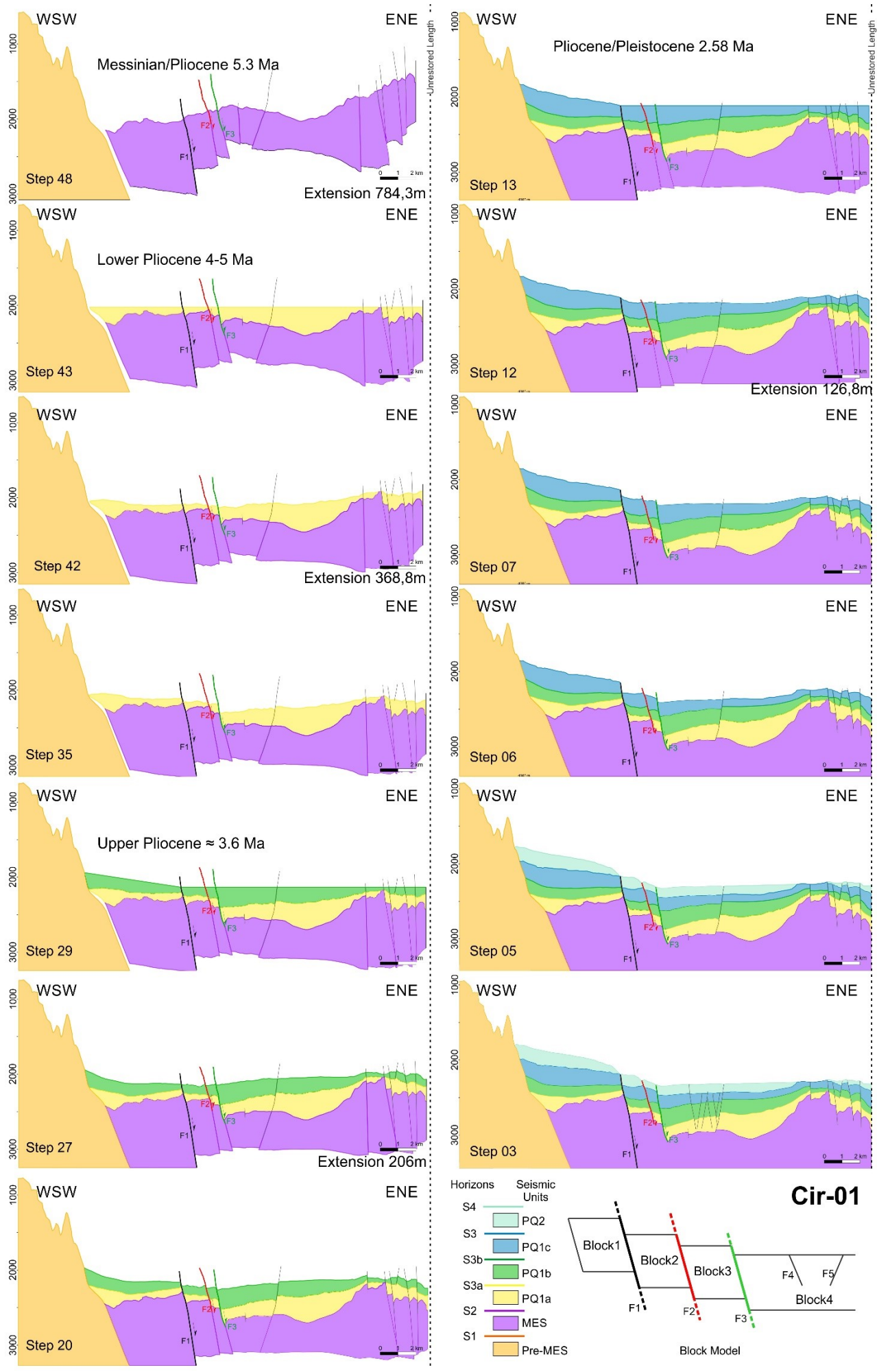


Fig.4

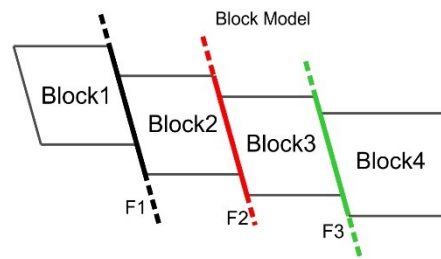
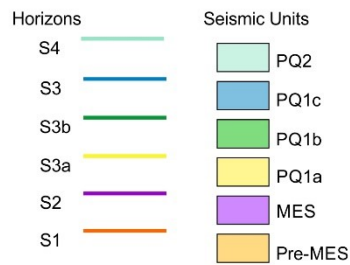
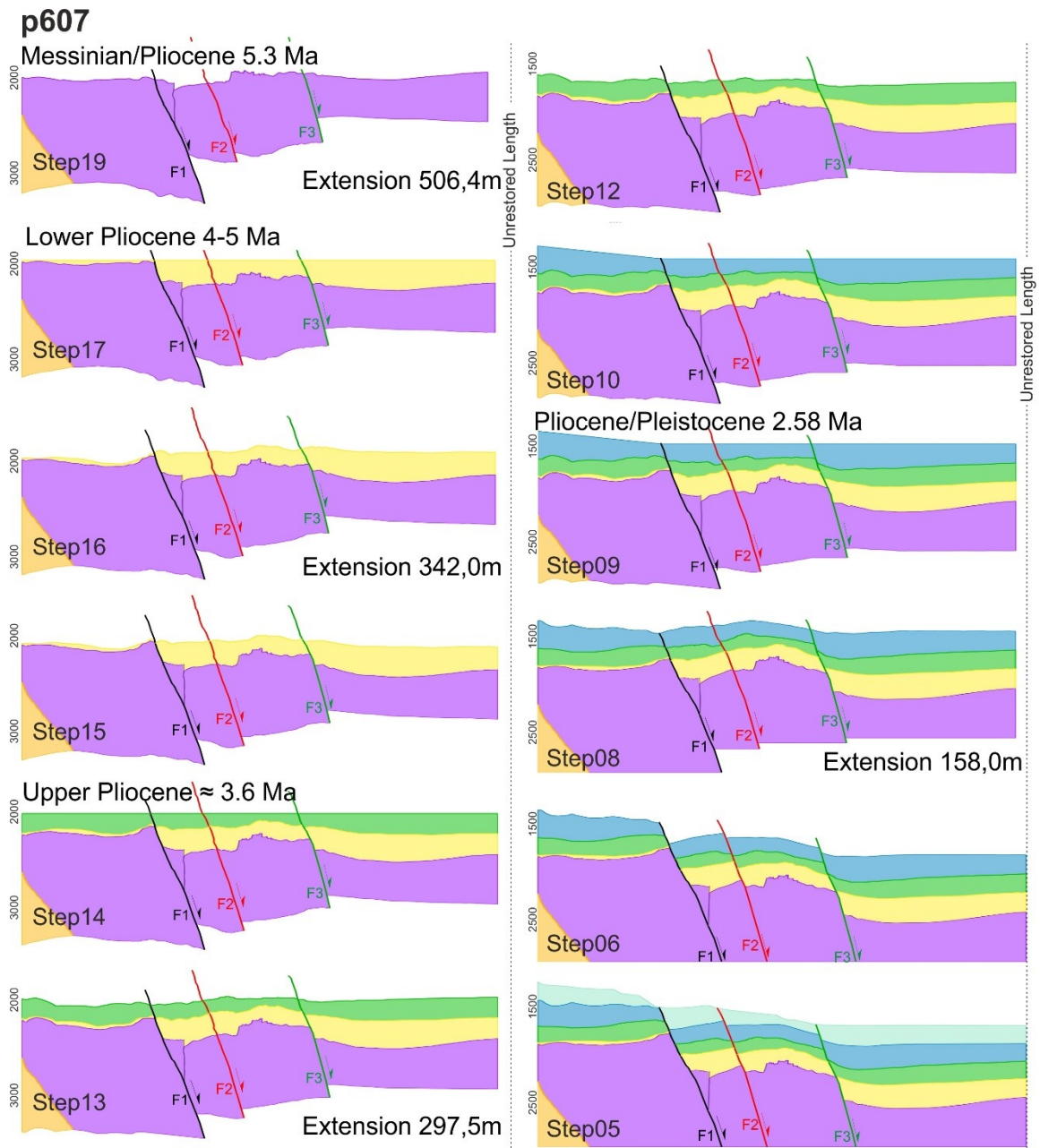


Fig.5

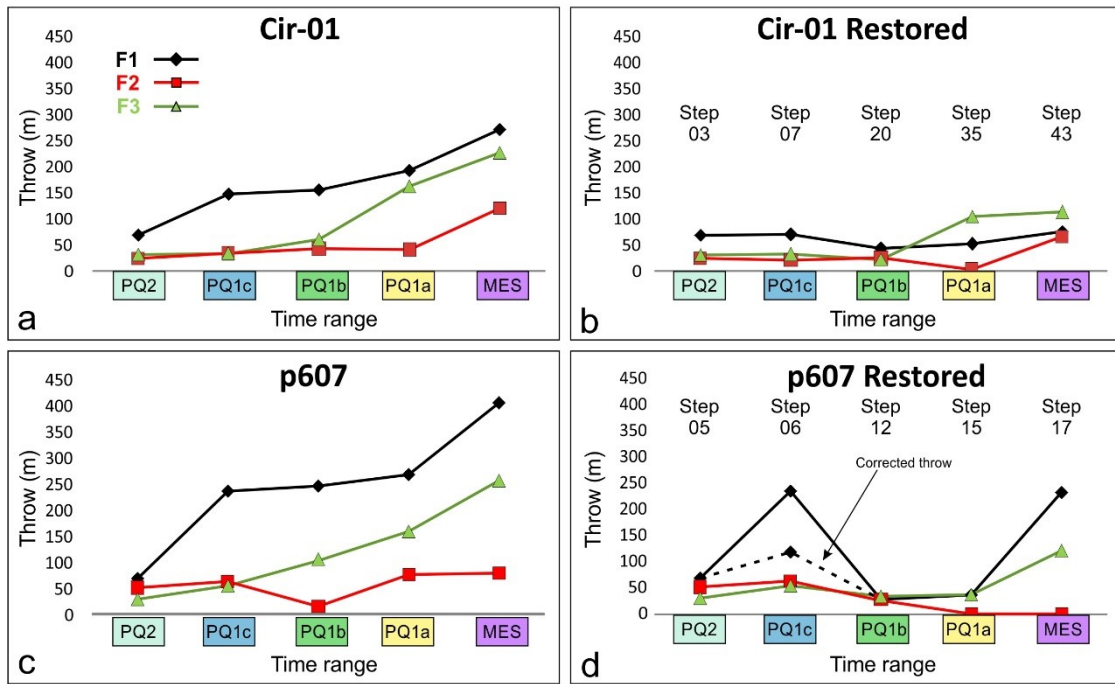


Fig.6

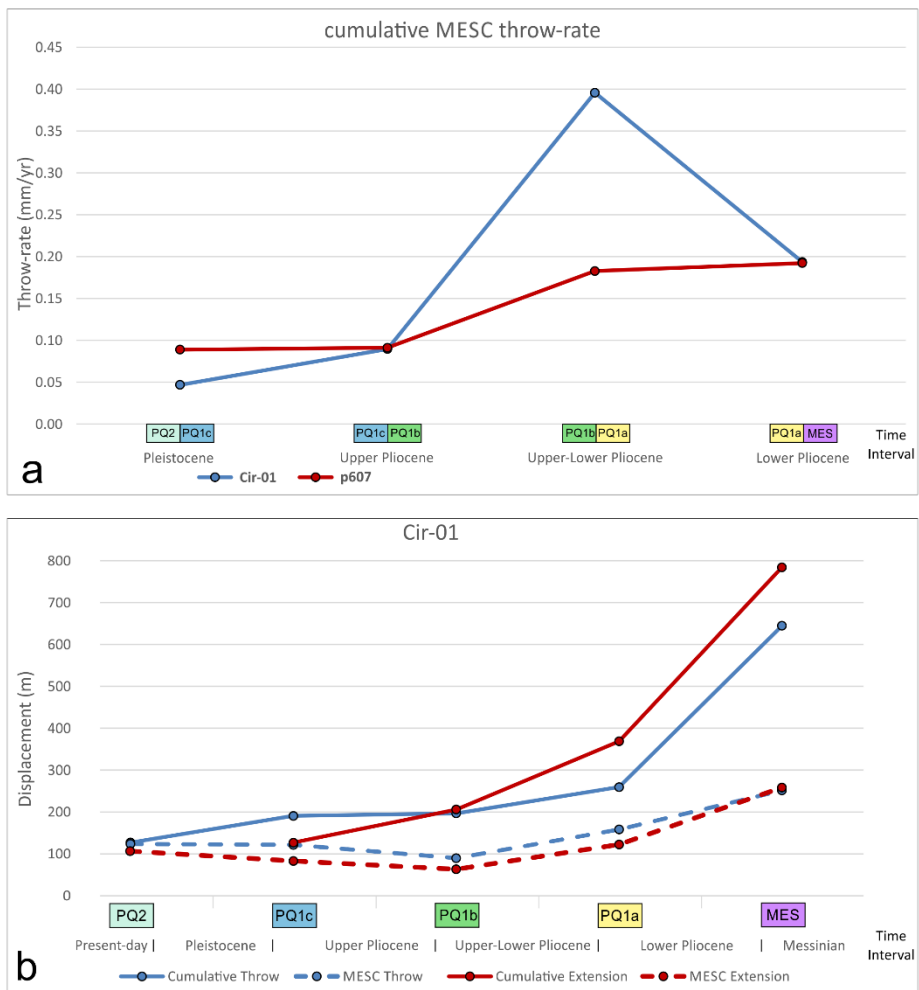


Fig.7

801
802
803

804
805
806
807

Seismic Unit	Age	Age (Ma)	Lithology	Seismic Velocity (m/s)	Surface porosity	Density (km/m ³)	Depth Coeff. (km ⁻¹)
PQ2	Quaternary	2.58-0.012	Silty-sandstones	1760	0.4	2700	0.39
PQ1c	Upper Pliocene	3.6-2.58	Silty-sandstones	2280	0.4	2700	0.39
PQ1b	Upper/Lower Pliocene	4.0-3.6	Silty-sandstones	2280	0.4	2700	0.39
PQ1a	Lower Pliocene	5.3-4.0	Silty-sandstones	2280	0.4	2700	0.39
MES	Messinian	7.2-5.3	Evaporites	4000	0	2200	0.00
Pre-MES	Pre-Messinian	> 7.2	Limestones	3250	0.7	2700	0.71

808

Tab 1

Cir-01

Restoration Step	Name	F1			F2			F3			MESC Extension	MESC Throw (m)	Cumulative Extension (m)
		Heave	Slip	Throw	Heave	Slip	Throw	Heave	Slip	Throw			
03	PQ2	50.72		68.30	27.40		24.10	26.79		31.40	104.92	123.80	NONE
	PQ1c	77.75	165.66	146.20	54.92	64.57	33.74	16.97	36.97	32.85	149.63	212.79	
	PQ1b	142.26	211.89	153.89	44.59	61.43	42.15	46.93	76.44	60.08	233.78	256.12	
	PQ1a	222.64	295.11	190.95	53.84	67.41	40.38	114.89	198.92	160.94	391.38	392.27	
	MES	283.69	392.69	268.79	109.95	165.89	119.13	282.63	365.62	224.56	676.26	612.48	
07-12	PQ1c	36.63	78.40	69.23	26.27	33.24	20.36	20.22	37.79	31.92	83.12	121.51	126.8
	PQ1b	109.50	168.31	125.34	45.16	63.56	44.61	46.29	77.14	61.47	200.96	231.42	
	PQ1a	222.66	294.86	190.56	48.77	61.59	37.48	117.44	206.65	168.39	388.86	396.43	
	MES	283.69	392.95	268.89	109.93	166.68	120.15	282.63	366.21	225.45	676.25	614.49	
20-27	PQ1b	25.77	49.76	42.54	21.47	32.67	24.58	16.03	27.72	22.61	63.27	89.73	206
	PQ1a	107.87	149.11	101.34	28.66	37.46	24.12	81.40	144.80	118.85	217.94	244.31	
	MES	191.87	255.50	166.65	90.01	133.96	94.37	238.54	317.55	203.68	520.43	464.69	
35-42	PQ1a	56.37	77.67	51.62	3.32	4.38	2.86	62.75	121.74	103.78	122.44	158.27	368.8
	MES	145.92	189.58	120.91	74.41	106.64	71.13	207.08	285.39	190.92	427.41	382.96	
43-48	MES	85.61	114.38	75.77	84.75	109.41	64.32	87.93	142.43	111.52	258.29	251.62	784.3

809

810

Tab.2a

p607

Restoration Step	Name	F1			F2			F3			Corrected Heave (m)				Corrected Throw (m)				Cumulative Extension (m)
		Heave	Slip	Throw	Heave	Slip	Throw	Heave	Slip	Throw	F1	F2	F3	Tot	F1	F2	F3	Tot	
05	PQ2	69.89		68.20	38.86		50.40	22.94		29.90	69.89	38.86	22.94	131.69	68.20	50.40	29.90	148.50	NONE
	PQ1c	199.41	310.20	235.63	48.56	78.66	61.84	35.30	65.73	55.39	120.73	48.56	35.30	204.59	117.82	61.84	55.39	235.05	
	PQ1b	210.04	324.84	245.36	11.84	19.52	15.52	71.29	128.89	105.88	210.04	11.84	71.29	293.17	245.36	15.52	105.88	366.77	
	PQ1a	244.09	363.43	267.23	56.84	93.55	74.30	156.50	222.85	158.46	244.09	56.84	156.50	457.43	267.23	74.30	158.46	499.99	
	MES	429.09	593.85	404.69	73.33	106.33	76.92	155.07	300.23	254.85	429.09	73.33	155.07	657.49	404.69	76.92	254.85	736.45	
06-08	PQ1c	199.40	307.37	231.69	48.56	78.26	61.31	35.24	63.99	53.36	118.71	48.56	35.24	202.51	115.84	61.31	53.36	230.52	158
	PQ1b	210.02	327.23	248.34	11.84	20.47	16.70	71.28	134.23	112.14	210.02	11.84	71.28	293.14	248.34	16.70	112.14	377.18	
	PQ1a	244.06	364.90	268.87	56.84	97.10	78.73	156.49	228.19	165.87	244.06	56.84	156.49	457.40	268.87	78.73	165.87	513.47	
	MES	429.05	595.73	407.22	73.33	106.81	77.59	155.11	300.85	255.11	429.05	73.33	155.11	657.49	407.22	77.59	255.11	739.92	
12-13	PQ1b	22.64	38.08	30.53	44.05	51.46	26.18	23.17	41.63	34.55	22.64	44.05	23.17	89.86	30.53	26.18	34.55	91.26	297.5
	PQ1a	47.28	95.55	82.55	15.70	21.81	15.14	72.57	103.59	73.92	47.28	15.70	72.57	135.54	82.55	15.14	73.92	171.61	
	MES	190.18	319.06	254.60	16.31	27.33	21.93	103.64	192.26	159.42	190.18	16.31	103.64	310.13	254.60	21.93	159.42	435.95	
15-16	PQ1a	45.29	58.28	36.56	0.00	0.00	0.00	45.29	58.28	36.56	45.29	0.00	45.29	90.57	36.56	0.00	36.56	73.12	342
	MES	170.75	287.74	229.57	0.00	0.00	0.00	87.86	150.49	119.50	170.75	0.00	87.86	258.61	229.57	0.00	119.50	349.07	
17-19	MES	132.80	228.00	183.50	0.00	0.00	0.00	62.30	91.40	66.40	132.80	0.00	62.30	195.10	183.50	0.00	66.40	249.90	506.4

811

812

Tab.2b

813

Cir-01										
Step	Unit	Cumulative Throw (m)	MESC Throw (m)	% Throw	MESC throw rate (mm/yr)	Cumulative Extension (m)	MESC Extension (m)	% Extension	Total Ext. Rate (mm/yr)	MESC Ext. Rate (mm/yr)
03	PQ2	127.00	123.80	97.48	12.38		104.92			10.49
07 - 12	PQ1c	190.89	121.51	63.65	0.05	126.80	83.12	65.55	0.05	0.03
20 - 27	PQ1b	196.80	89.73	45.59	0.09	206.00	63.27	30.71	0.21	0.06
35 - 42	PQ1a	259.38	158.27	61.02	0.40	368.80	122.44	33.20	0.92	0.31
43 - 48	MES	644.62	251.62	39.03	0.19	784.30	258.29	32.93	0.60	0.20

814

815

816

Tab.3a

p607					
Step	Unit	MESC Throw (m)	MESC Throwrate (m)	MESC Extension (m)	MESC Ext. Rate (mm/yr)
05	PQ2	148.50	14.85	131.69	13.17
06 - 08	PQ1c	230.52	0.09	202.51	0.08
12 - 13	PQ1b	91.26	0.09	89.86	0.09
15 - 16	PQ1a	73.12	0.18	90.57	0.23
17 - 19	MES	249.90	0.19	195.10	0.15

817

818

819

820

821

822

823

824

Tab.3b